

Hestia: Hierarchical Next-Best-View Exploration for Systematic Intelligent Autonomous Data Collection

Cheng-You Lu

University of Technology Sydney
cheng-you.lu@student.uts.edu.au

Zhuoli Zhuang

University of Technology Sydney
zhuoli.zhuang@student.uts.edu.au

Nguyen Thanh Trung Le

University of Technology Sydney
nguyenthanhtrung.le@student.uts.edu.au

Da Xiao

University of Technology Sydney
da.xiao@uts.edu.au

Yu-Cheng Chang

University of Technology Sydney
fred.chang@uts.edu.au

Thomas Do

University of Technology Sydney
thomas.do@uts.edu.au

Srinath Sridhar

Brown University
srinath@brown.edu

Chin-Teng Lin

University of Technology Sydney
chin-teng.lin@uts.edu.au

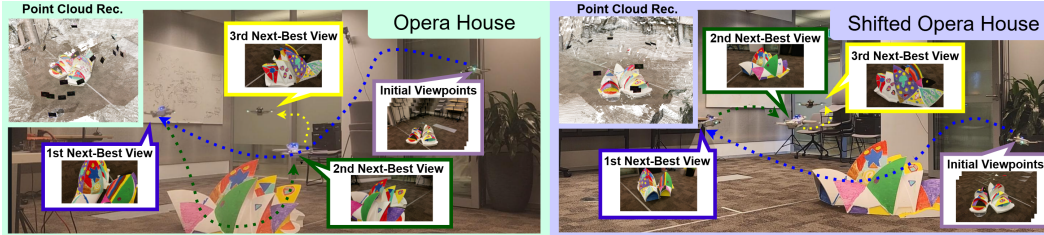


Figure 1: **Data collection system.** Hestia is an intelligent data collection system that integrates a next-best-view planner with a drone-based real-world platform, enabling robust viewpoint prediction even under spatial shifts of objects. *Please refer to our demonstration video for further details.*

Abstract: Advances in 3D reconstruction and novel view synthesis have enabled efficient, photorealistic rendering, but the data collection process remains largely manual, making it time-consuming and labor-intensive. To address the challenges, this study introduces Hierarchical Next-Best-View Exploration for Systematic Intelligent Autonomous Data Collection (Hestia¹), which leverages reinforcement learning to learn a generalizable policy for 5-DoF next-best viewpoint prediction. Unlike prior approaches, Hestia systematically defines the next-best-view task by proposing core components such as dataset choice, observation design, action space, reward calculation, and learning schemes, forming a foundation for the planner. Hestia goes beyond prior next-best-view approaches and traditional capture systems through integration and validation in a real-world setup, where a drone serves as a mobile sensor for active scene exploration. Experimental results show that Hestia performs robustly across three datasets and translated object settings in the NVIDIA IsaacLab environment, and proves feasible for real-world deployment. *The code and data processing script for Hestia are included in the supplementary materials and will be released after the paper is published.*

¹In Greek mythology, Hestia is the goddess of the hearth, symbolizing home, foundation, and structure, representing stability and guidance in complex systems

1 Introduction

Throughout the years, multiview-based 3D scene reconstruction [1, 2, 3, 4, 5, 6, 7, 8, 9, 10, 11, 12, 13, 14, 15] and novel view synthesis [16, 17, 18, 19, 20, 21, 22, 23, 24, 25, 26, 27, 28, 29, 30] have been critical research fields in computer vision and graphics. These methods leverage multiview information (e.g., correspondences) from images to reconstruct high-fidelity scenes or synthesize photorealistic novel views. However, collecting multiview data is often time-consuming and labor-intensive, as these methods usually depend on manually captured data. The situation becomes more challenging for generalizable approaches [17, 23, 24, 26, 29, 30, 31] that require diverse and extensive data [31, 32, 33, 34, 35]. From a data collection perspective, one way to reduce the effort is to develop machines (e.g., multiview camera rigs) [36, 37, 38, 39, 40, 41, 42] to minimize human intervention. Although these machines make the data collection process more scalable, their sensors are usually passive (e.g., non-movable), lacking the ability to actively explore the scene. This lack of active exploration may result in missing occluded parts. To enable active capture and alleviate the effort required for manual capture, we propose Hestia, a Hierarchical Next-Best-View Exploration for Systematic Intelligent Autonomous Data Collection. The goal of Hestia is to actively collect data from object-centric scenes with a higher coverage ratio and less amount of data, demonstrating that the proposed prototype has the potential to operate in real-world settings. We address this problem by introducing two main modules, which are a next-best-view planner (see Sec. 3) that actively determines a five-degree-of-freedom (5 DoF) viewpoint (e.g., camera position, yaw, and pitch) based on voxel face observations and an intelligent data collection system (see Sec. 4) that uses a drone equipped with an RGB camera as the agent for data collection.

In recent decades, next-best-view planners have been developed for active capture, demonstrating promising potential for reducing the human workload. This is particularly important when a professional human pilot is unavailable to control the robot (e.g., a drone), or when human resources are limited or urgently needed elsewhere. Traditional next-best-view planners [44, 45, 46, 47, 48] rely on heuristic rules to predict the viewpoint. Although these approaches show promising and awesome performance for specific scenarios, the same handcrafted rules or hyperparameters may not be the best setting for other scenes as discussed by [43]. Thanks to advancements in deep learning and computational capabilities, several learning-based (e.g., online learning or generalizable methods) next-best-view planners [43, 49, 50, 51, 52, 53, 54, 55, 56, 57, 58] have been developed. Among these approaches, a generalizable RL-based method [43] that utilizes an occupancy grid as the observation demonstrates effective performance in terms of coverage ratio, viewpoint flexibility, and generalization capability.

Inspired by the approach [43], we develop a next-best-view planner utilizing a voxel grid as the observation. Unlike the prior work [43], our method introduces a concept, *“A voxel is worth more than a ray”*, by incorporating the visibility of the six faces of each voxel into the observation and reward function (see Fig. 2 and Sec. E). Theoretically, if we keep sampling with a 1-ray camera in a scene containing k unit cubes, then from a coupon collector’s perspective [59], treating each voxel as a point will result in approximately $k^{-\frac{1}{6}}$ of the faces being missed when sampling stops (see appendix Sec. A). In contrast, treating each voxel as a cube allows faces to be fully covered. Hence, Hestia accounts for the visibility of individual voxel faces and achieves

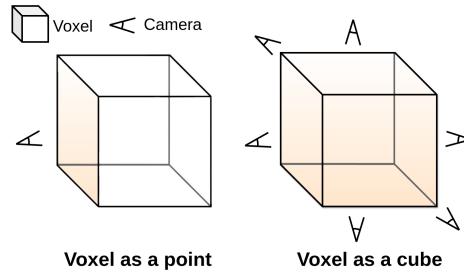


Figure 2: A voxel is worth more than a ray. Unlike the RL-based generalizable method [43], Hestia treats each voxel as a cube by considering its six faces, rather than a point. This reduces the information loss inherent in point approximations, ensuring a more accurate representation of the voxel.

more comprehensive data capture. In addition, representing each voxel as a cube does not introduce significant computational overhead and still enables real-time operation at 25 FPS (see Tab. 1).

To further help the learning process, Hestia focuses on three key aspects of generalizable RL: the observation (e.g., the diversity and scale of the dataset), the action (e.g., the dimension of the action space), and the learning process (e.g., strategies for training). For observation, Hestia utilizes the largest dataset processed from Objaverse [60, 61], for the next-best-view task (see Sec. I). Therefore, Hestia encounters a more diverse range of surface geometries, rather than just cubic shapes (see Sec. I). For action, instead of directly predicting the 5 DoF next-best viewpoint, a task that is inherently complex and challenging, Hestia adopts a hierarchical structure to simplify the process. The approach begins by predicting the look-at point, which serves as the target of focus, followed by determining the viewpoint position based on this point. Finally, Hestia formulates the next-best-view task as a greedy optimization problem. Given an occupancy grid, the goal is to find the viewpoint that maximizes the coverage ratio. To achieve this, Hestia relies solely on the previous image, camera pose, and the given occupancy grid to predict the next-best-view, rather than depending on a sequence of images [43, 55] and camera poses [43]. Additionally, the reward discount factor γ is set to a small value to prioritize current improvements without relying on a disproportionately large goal reward. Following a greedy algorithm, Hestia can mitigate the spurious correlations² (see Fig. A7) arising from false associations between the current action and a large future reward (e.g., the final goal reward). Hence, Hestia can reach a better coverage ratio with fewer images than previous methods [43, 53, 55].

The proposed next-best-view planner is integrated into an intelligent data collection system, with the planner running on a ground station, to demonstrate its effectiveness in real-world scenarios. The system employs a drone as an agent, equipped with a camera mounted on a gimbal, to capture data. Using drones instead of robot arms [51] practically enables data collection in regions that are difficult for humans to access. The contributions of this work are:

- A generalizable RL-based next-best-view planner achieves a better coverage ratio with fewer images by explicitly considering voxels as cubes rather than points.
- Propose a hierarchical structure to handle the high-dimensional action space, use the largest dataset to ensure robustness, and adopt a greedy algorithm to reduce spurious correlations.
- Integrate the next-best-view planner into an intelligent, autonomous data collection prototype to demonstrate its potential for active data capture under real-world scenarios.

2 Related Work

Data collection systems. Advances in 3D reconstruction [8, 9, 10, 11, 12, 13, 14, 15, 64, 65, 66] and novel view synthesis [16, 17, 18, 19, 20, 21, 22, 23, 24, 25, 26, 27, 28, 29, 30, 67, 68, 69, 70, 71, 72] techniques have enabled the rendering of high-fidelity and photo-realistic scenes. However, most approaches depended on manually captured data [39, 73, 74, 75], which is both time-consuming and labor-intensive. This limitation makes the data collection process less practical for generalizable approaches [13, 14, 17, 23, 24, 26, 29, 30, 31, 66, 70, 71, 72]. To overcome this, some methods [31, 34, 35, 60, 61, 76, 77] collected data from the internet, leveraging contributions from people worldwide. While these approaches enable the rapid collection of large datasets and benefit generalizable methods, they face potential drawbacks such as inconsistent data quality and the risk of saturation due to the inability to generate their own data. Instead, many people developed their data collection machines [36, 37, 38, 39, 40, 41, 78, 79, 80] to capture high-quality data, which is a more sustainable approach in the long term. For instance, multiview camera rigs have been used to capture face-forward scenes [37, 38, 39, 40, 80], 360° outward-facing scenes [36], and 360° inward-facing scenes [41]. Other studies [79] have combined multiple camera devices (e.g.,

²Spurious correlations [62, 63] refer to certain groups contributing to model errors. In this study, spurious correlations refer to large positive future rewards assigned to suboptimal current next-best-view decisions, leading to ineffective policy learning.

spectacles camera and 360° camera) to capture scenes from different perspectives. Additionally, ego-centric approaches [78] developed wearable camera glasses to collect data from a first-person perspective while the user was in motion. Although these methods can collect large amounts of data using multiple cameras or passively gather data through human-operated devices, they lack the capability to actively explore the scene. In contrast, our proposed data collection system is intelligent, enabling autonomous exploration of the scene using a drone as a mobile sensor.

Scene-specific next-best-view planners. Next-best-view planners have demonstrated promising results in active 3D reconstruction by predicting the optimal viewpoint for data capture based on the current state. Traditional approaches [44, 45, 46, 47, 48] rely on hand-crafted rules to determine the next-best viewpoint. For instance, the method [45] selected the next-best viewpoint by maximizing a rating function favoring smooth regions, which may overlook fine-grained object details. Instead, the methods [44, 47] collected data along boundaries between seen and unseen surfaces to capture finer details, but still require handcrafted parameter tuning for each scene. Another approach [46] scanned segmented objects sequentially using a predefined object database, reducing the need for handcrafted tuning, but its performance degrades in cluttered environments due to inaccurate object matching. Recent advances in deep learning and increased computational power have given rise to learning-based methods [43, 49, 50, 51, 52, 53, 54, 55, 56]. Some studies [49, 54] used NeRF [16] ensembles to estimate uncertainty via model disagreement for viewpoint selection, resulting in linearly increasing computational overhead. Other works [50, 56] avoid the computational overhead by incorporating Bayesian-based NeRF [81, 82] to estimate uncertainty for viewpoint selection. Meanwhile, other approaches [51, 52] defined the next-best viewpoint as the viewpoint that maximizes the entropy of the density field along the camera rays. Although these methods have shown outstanding performance in collecting data, all require sampling candidate viewpoints. In addition, their reliance on online learning makes them less suitable for real-time applications.

Generalizable next-best-view planners. Unlike the aforementioned online-learning approaches, the generalizable methods [43, 53, 55] avoid the training process for new scenes, thereby enabling faster next-best-view selection. The prediction time is important for real-world tasks where a robot (e.g., a drone) may run out of battery within a few minutes. Among generalizable methods, prior work [53] proposed a Bayesian-based NeRF that selects the next-best viewpoint to maximize view variance without additional training. However, it still requires candidate viewpoint sampling, resulting in non-real-time performance. Instead, another line of generalizable next-best-view approaches [43, 55] utilized reinforcement learning (RL) to learn a next-best-view planner to bypass the need for sampling candidate viewpoints. Prior work [55] proposed learning a 3-DoF next-best-view policy using a series of grayscale images as observations. Subsequently, prior work [43] improved upon this method by incorporating occupancy grids into the observations, which provide explicit geometric information. This enhancement enabled the development of a 5-DoF next-best-view planner, achieving an outstanding coverage ratio for unknown scenes.

As shown in Tab. A4, compared to scene-specific methods, Hestia does not require candidate viewpoint sampling or inference-time optimization, thereby enabling more flexible viewpoint prediction. Compared to the generalizable method [43], Hestia treats voxels as cubes rather than points, enabling more comprehensive capture. In addition, Hestia adopts a greedy scheme to mitigate spurious correlations, introduces a hierarchical structure to model the action space, and uses a more diverse dataset to maintain robust performance across varying object shapes and positions.

3 Methods

3.1 RL Problem Definition

Our next-best-view task is to identify a 5-DoF viewpoint that maximizes the coverage ratio of an incomplete occupancy grid of the scene. The task’s goal is similar to greedy methods, which always seek the locally optimal solution. We formulate the problem as a Markov Decision Process (MDP), denoted by the tuple $\{S, A, P, R, \gamma\}$. At each time step t , the agent with an RGB-D camera observes a state s_t from the set of all possible states S and chooses an action a_t from the action space A . The

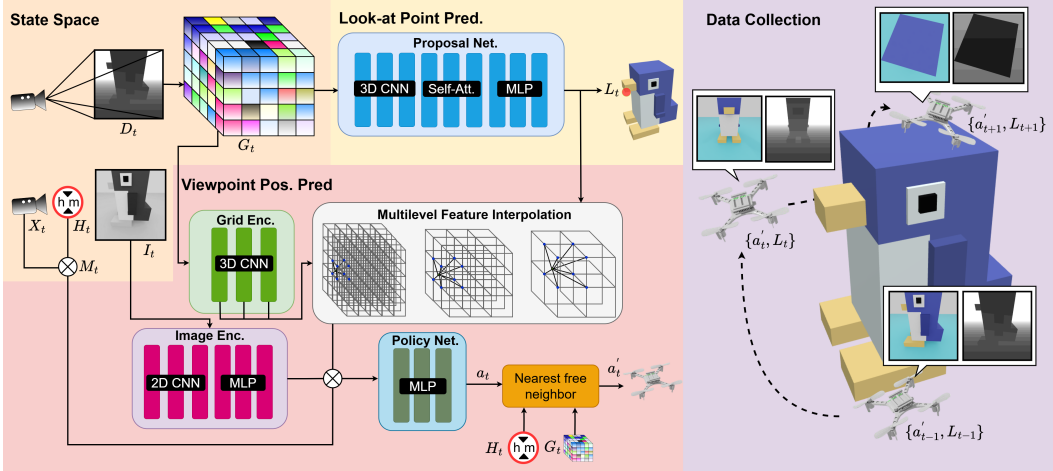


Figure 3: **Hierarchical structure of Hestia.** Hestia first predicts the camera’s look-at point L_t using a proposal neural network that takes grid information G_t processed from the depth image D_t and the camera pose as input. Next, Hestia employs a grid encoder to encode the grid information G_t and performs trilinear interpolation to extract corresponding features from the encoded grid at different layers based on L_t . These multilevel interpolated features are then concatenated with the vector information M_t which includes the camera pose X_t and the maximum flyable height, H_t as well as the encoded image features. The image features are extracted using an image encoder, which takes the grayscale image I_t as input. Finally, this combined feature representation is fed into the RL policy model to predict the camera’s position a_t . Note that Hestia adopts a'_t , the nearest collision-free point to a_t , as the final camera position to ensure a collision-free viewpoint. Hence, the next-best viewpoint $\{a'_t, L_t\}$ is used for data collection.

environment then transitions to the subsequent state s_{t+1} according to the probabilities described by P , and provides a reward r_t . The magnitude of this reward is determined by the reward function $R(\cdot | s, a) : S \times A \rightarrow r$. In reinforcement learning (RL), the main goal is to discover an optimal policy π that maximizes the expected sum of discounted rewards, given by $E_t = \sum_{k=0}^{\infty} \gamma^k r_{t+k}$, where $\gamma \in (0, 1)$ is the discount factor. We set γ to 0.1 to align with the greedy-like objective and to avoid spurious correlations from large positive future rewards (see Fig. A7).

State space. The state space of Hestia is defined as $S = \{s_t \mid s_t = \{I_t, M_t, G_t, L_t\}, t \in \mathbb{N}\}$, where $I_t \in \mathbb{R}^{h \times w}$ is the grayscale image with height h and width w , and $L_t \in \mathbb{R}^3$ is the camera look-at point. The vector $M_t \in \mathbb{R}^6$ consists of $X_t \in \mathbb{R}^5$, which is the camera position, pitch, and yaw, as well as $H_t \in \mathbb{R}^1$, representing the maximum flyable height for the capture. Meanwhile, $G_t \in \mathbb{R}^{g \times g \times g \times 10}$ includes the aggregated grid information at resolution g , consisting of $O_t \in \mathbb{R}^{g \times g \times g \times 1}$ for the cumulative occupancy grid, $C_t \in \mathbb{R}^{g \times g \times g \times 3}$ for the positional encoding, and $F_t \in \{0, 1\}^{g \times g \times g \times 6}$ for the cumulative face visibility. The cumulative face visibility is updated iteratively as $F_t = f_t \vee F_{t-1}$, where F_t represents the cumulative face visibility for all voxels up to time t , and $f_t \in \{0, 1\}^{g \times g \times g \times 6}$ denotes the current face visibility. To compute f_t , the depth image D_t is unprojected into a voxelized point cloud $V = \{v_i \mid i \in \mathbb{N}\}$, where v_i is the i -th voxel. Each voxel v_i is associated with a viewing direction vector $d_{v_i} \in \mathbb{R}^3$, defined as the vector pointing from the voxel center to the collision-free camera position a_t . The vector \mathbf{d}_{v_i} is computed as $\mathbf{d}_{v_i} = \frac{a'_t - p_{v_i}}{\|a'_t - p_{v_i}\|}$, where p_{v_i} is the center of voxel v_i . For each voxel v_i and its six outward-facing face normals $n_{i,j} \in \mathbb{R}^3$, the face visibility is determined and aggregated as

$$f_t(v_i, j) = \mathbb{1}(d_{v_i} \cdot n_{i,j} > 0), \quad \forall v_i \in V, j \in \{1, \dots, 6\} \quad (1)$$

where $\mathbb{1}(\cdot)$ is the indicator function. By iterating over all voxels and their respective faces, f_t is constructed, and the cumulative visibility F_t is updated accordingly. Although this method cannot handle all face visibilities, the approximation enables efficient computation of face visibility. Unlike

prior works [43], which consider only O_t and C_t and thereby treat voxels as points, we treat voxels as cubes to mitigate the information loss caused by approximating voxels as points (see Fig. 2). For details regarding O_t and C_t , please refer to the work [43].

Action space. The action space $A = \left\{ a_t \mid a_t \in [-1, 1]^3, t \in \mathbb{N} \right\}$ represents the set of possible 3-DoF viewpoints (e.g., camera positions) at each time step t , where each coordinate is initially bounded within $[-1, 1]$. These coordinates are subsequently normalized to the environment’s scale to ensure appropriate positioning within the scene. Additionally, the camera’s pitch and yaw are derived from the look-at point and the collision-free action a'_t converted from a_t (see Sec. 3.2).

Reward. The reward function is defined as $r_t = R(s_t, a_t) = r_{\text{coverage}}(s_t, a_t) + r_{\text{constraint}}(s_t, a_t)$, where $r_{\text{coverage}}(s_t, a_t)$ encourages the observation of new voxel faces and is expressed as

$$r_{\text{coverage}}(s_t, a_t) = \frac{\sum_{i=1}^N \sum_{j=1}^6 \left(F_t^{i,j} - F_{t-1}^{i,j} \right) \cdot M_{\text{col}}}{N \cdot 6} \cdot 0.3 \quad (2)$$

where $F_t^{i,j}$ and $F_{t-1}^{i,j}$ represent the visibility status of the j -th face of the i -th voxel at time t and $t - 1$, respectively. Here, $M_{\text{col}} \in \{0, 1\}$ is a collision indicator, set to 0 in the event of a collision, thereby preventing any positive reward for invalid actions. The term $r_{\text{constraint}}(s_t, a_t) = -0.01$ is applied when unsafe or invalid actions occur (see Sec. E for details). Our reward is based on the face coverage ratio rather than the point coverage ratio to ensure more comprehensive capture (see Fig. 2). Furthermore, to prevent spurious correlations, the reward design aligns with a greedy-like objective, which differs significantly from prior works [43, 55] that provide a large goal reward when the coverage ratio reaches a predefined target.

3.2 Next-Best-View Hierarchical Network

The goal of the task is to predict a 5-DoF viewpoint for data collection. Directly modeling the 5-DoF viewpoint in the RL continuous action space is challenging due to the high-dimensional search space. To address this, Hestia introduces a hierarchical structure to simplify the problem.

Look-at point prediction. Hestia first predicts the look-at point using a proposal network (see Fig. 3), which takes grid information G_t as input to determine *where to look*. The proposal network is a 3D convolutional neural network with a self-attention layer to expand the receptive field. The output is then passed through linear layers to decode the look-at point L_t . To model the look-at point as a probability distribution, the reparameterization trick is used, treating it as a sample from a normal distribution.

Viewpoint position prediction. To predict the remaining 3-DoF viewpoint position (e.g., *where to fly*), the grid information is encoded into a multilevel feature grid using a shallow 3D CNN. The look-at point L_t is then used to perform trilinear interpolation on the multilevel features from the grid. These interpolated features are concatenated with the image embedding, which is extracted by an image encoder, a shallow CNN that takes the grayscale image I_t as input. Additionally, the features are concatenated with vector information M_t , which includes the camera pose X_t and the maximum flyable height H_t . The combined features are fed into the RL policy model to predict the action a_t . While the reward function helps constrain a_t to avoid collisions, an additional constraint is applied to ensure a collision-free viewpoint. Specifically, a_t is shifted to its nearest collision-free point a'_t determined using G_t and H_t . This adjusted action a'_t serves as the final viewpoint position for data capture. Thus, Hestia’s next-best-view is represented as $\{a'_t, L_t\}$.

Training loss functions. The look-at point and viewpoint prediction networks can be jointly trained using the *RL reward* due to their connection. However, our previous experiments showed no clear benefit from joint training using the *RL reward*. To simplify the design, we detach the gradient flow between the networks and train the look-at point prediction network with supervised learning using ground-truth targets. The ground truth look-at point L_t^{gt} is computed as the weighted average position of the ground truth uncaptured surface $L_t^{\text{gt}} = \frac{\sum_{v_i \in U} w_{v_i} p_{v_i}}{\sum_{v_i \in U} w_{v_i}}$, where U represents the set of voxels containing ground truth uncaptured faces, and $w_{v_i} = \sum_{f \in F_{v_i}^{\text{gt}}} 1$ is defined as the total number



Figure 4: **Proposed data collection system and processes.** Hestia goes beyond prior works by introducing an intelligent system using a drone with an RGB camera for data capture, Lighthouse base stations and Crazyflie for localization, and a Wifi router for wireless communication.

of ground truth uncaptured faces within voxel v_i where $F_{v_i}^{\text{gt}}$ is the set of ground truth uncaptured faces associated with voxel v_i . Thus, the loss function for the proposal network is formulated as $\mathcal{L}_{\text{proposal}} = \|L_t - L_t^{\text{gt}}\|^2$. The loss of the viewpoint prediction network is the same as the regular RL loss \mathcal{L}_{RL} which depends on the RL method used, combined with an auxiliary loss $\mathcal{L}_{\text{aux}} = \|a_t - a'_t\|^2$ to encourage the predicted action a_t to align with the collision-free action a'_t . Hence, the overall loss function for Hestia is $\mathcal{L}_{\text{all}} = \mathcal{L}_{\text{RL}} + 0.5 \cdot \mathcal{L}_{\text{aux}} + \mathcal{L}_{\text{proposal}}$.

4 Real-world Data Collection System

To demonstrate our work, we propose a real-world system (see Fig. 4), where a drone equipped with an RGB camera moves to the next-best viewpoint predicted by Hestia to capture images of an object. The system uses four HTC Lighthouse base stations and a Crazyflie 2.1 for localization and transmits images to the ground control station via wireless communication. MAS3R [14] is integrated to convert RGB images into pointmaps (e.g., depth images), and three initial viewpoints are set for real-world and virtual-world synchronization [83]. Fig. 4 illustrates four key processes of the system. Specifically, the drone captures images at three initial viewpoints, where the *set waypoints process* navigates the drone using a heuristic trajectory planner based on prior knowledge of the environment. Then, the *capture image process* commands image capture, and the *receive image process* transmits the image to the ground station. After capturing the initial viewpoints, the *nbv prediction process* predicts the next-best viewpoint based on the collected data. Four processes repeat until sufficient data is collected. For more details, please refer to Sec. J.

5 Experiments

5.1 Experimental Setup

Hestia is trained on our processed Objaverse [60, 61] split to showcase its capability and on our Houses3K [55] split denoted as Hestia-H3K for fair comparison. We use NVIDIA IsaacLab [84] to simulate 256 scenes in parallel, with each object scaled up to 8 meters and placed in a $20 \times 20 \times 20$ m scene. Objects are randomly translated during training and placed at the origin and the four corners for benchmarking. An RGB-D camera is ahead of the Crazyflie drone, which starts from a random collision-free position oriented toward the object center. See Sec. I and Sec. K for more details.

5.2 Results

Quantitative and qualitative results. We compare Hestia with generalizable next-best-view approaches [43, 53, 55], using three metrics, coverage ratio (CR) [43], Chamfer Distance (CD), and the area under the coverage curve (AUC) [43] on point cloud reconstruction task. Online learning approaches are excluded due to non-real-time speed and limited computational resources. Evaluations are conducted on the OmniObject3D [85], Objaverse [60, 61], and Houses3K [55] test splits. Please refer to Sec. I for details of the datasets. As shown in Tab. 1, Hestia and Hestia-H3K outperform the

Train Data	Method	OmniObject3D	Objaverse	Houses3K	FPS
DTU	NeU-NBV [53]	77 / 48 / 73	79 / 33 / 75	78 / 38 / 75	<1
Houses3K	ScanRL [55]	80 / 32 / 75	81 / 27 / 78	81 / 32 / 76	15
	GenNBV [43]	93 / 12 / 87	91 / 14 / 86	92 / 14 / 87	26
	GenNBV (Rep.) [43]	93 / 11 / 87	92 / 13 / 86	94 / 12 / 89	27
	Hestia-H3K	96 / 6 / 93	95 / 8 / 91	97 / 7 / 96	25
Objaverse	Hestia	97 / 4 / 93	96 / 7 / 92	97 / 6 / 94	25

Table 1: **Overall performance on OmniObject3D, Objaverse, and Houses3K with 30 images per object.** Results are reported as mean CR (%), CD (cm), and AUC (%) over five object center positions. Both Hestia and Hestia-H3K outperform prior approaches by at least 3% in CR and AUC.

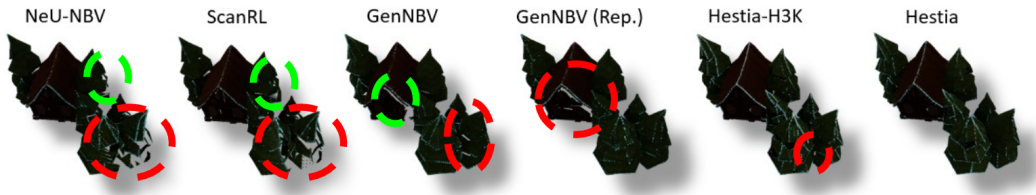


Figure 5: **Reconstruction on a complex scene.** Hestia and Hestia-H3K capture the scene well.

baseline [43] by at least 3% in both CR and AUC, and their CDs are nearly half of those of the baseline [43] across all three datasets, demonstrating a substantial improvement. Surprisingly, Hestia achieves slightly better CD than Hestia-H3K, even when the latter is evaluated on its in-distribution dataset (Houses3K), further validating the benefit of using a more diverse dataset. Hestia’s superior performance on other datasets also suggests that training on larger and more diverse data enhances robustness to varying object shapes. In addition, Hestia and Hestia-H3K surpass other baselines, indicating that treating voxels as cubes, using a hierarchical action space, and mitigating spurious correlations collectively improve performance. Tab. A1, Tab. A2, and Tab. A3 show that Hestia and Hestia-H3K maintain consistent performance, with less than a 1% drop in CR across different object positions. This demonstrates the effectiveness of the look-at point predictor, derived from the proposed hierarchical structure. The reconstructed point cloud using depth images collected by Hestia, shown in Fig. 5, demonstrates that Hestia and Hestia-H3K perform well in complex scenarios with multiple objects, while other methods miss occluded parts such as the leaves of the tree or the roof soffit. Fig. A1, Fig. A2, and Fig. A3 show additional qualitative results. Hestia successfully captures diverse object shapes, ranging from daily objects to building-like structures. These results highlight Hestia’s ability to handle challenging scenarios with occlusions and fine details. In addition, our ablation study in Sec. H validates the importance and effectiveness of combining the proposed components, and the visualization results in Sec. G validate that the greedy-like training scheme can mitigate spurious correlations in our task. With all these components, Hestia achieves superior performance. Please refer to Sec. B and Sec. C for more details on the qualitative and quantitative results, and to Sec. A, Sec. F, Sec. G, Sec. I, and Sec. H for more details on the importance of the proposed components.

Real-world demonstration. We demonstrate Hestia in the proposed data collection system (see Sec. 4 and Sec. J) across several scenes (see Sec. D). Hestia actively and autonomously explores the scene starting from three initial viewpoints, using a drone equipped with an RGB camera as a mobile sensor. Fig. A5 shows that Hestia captures both shifted and non-shifted scenes well, while Fig. A6 demonstrates that Hestia performs well across diverse real-world object shapes. These results show that Hestia goes beyond prior works, which typically remain limited to simulation environments (see Sec. F), and demonstrate the feasibility of developing Hestia for real-world applications.

6 Conclusion

We present Hestia, hierarchical next-best-view exploration for systematic intelligent autonomous data collection. Hestia addresses high-dimensional viewpoints by separately predicting look-at points and camera positions. Treating voxels as cubes enables more comprehensive capture, improving coverage ratios. The greedy design mitigates spurious correlations, ensuring efficient policy learning. Trained on a more diverse dataset, Hestia is robust across varied scenarios. The integration into a real-world drone-based data collection system highlights its feasibility. We hope Hestia inspires future advancements in scalable 3D reconstruction and autonomous exploration.

7 Limitations

There are some limitations to Hestia. In particular, in real-world scenarios, Hestia, like other real-world systems, is typically constrained by hardware, budget, and safety regulations. We hope that the research community works together to prevent the misuse of artificial intelligence, strengthen the development of AI safety regulations, and reduce public concerns regarding the deployment of AI technologies. Hence, the goal of this section is to comprehensively elaborate on the limitations of Hestia, particularly in real-world applications, to help prevent potential misuse.



Figure 6: **Failure cases of Hestia.** Hestia may occasionally fail to capture finer 3D structures, highly self-occluded parts, nearly vertical bottom-up views, and small details on coarse object surfaces.

Due to hardware limitations (e.g., the absence of an RGB-D camera), Hestia cannot fully exhibit its potential in real-world scenarios. However, since our system integrates a depth estimator to convert RGB images into depth maps, this limitation represents a tradeoff rather than a fundamental constraint. Our experiments conducted in NVIDIA IsaacLab demonstrate the full capability of Hestia, while our real-world data collection system highlights Hestia’s robustness when a depth sensor is unavailable. Another limitation of this work is that the drone’s path planner relies on heuristic rules derived from prior knowledge of the scene. Using occupancy grids for navigation in real-world scenarios presents additional challenges, as the grid is generated from RGB images rather than RGB-D data, increasing the risk of inaccuracies. A potential improvement would be to incorporate an on-line path planner. However, this approach would require onboard computing for real-time planning, necessitating the use of a customized drone. Hence, a potential future step to address the above

limitation is to build a customized large drone with improved payload capacity, equipped with an onboard computer and an RGB-D sensor mounted on a gimbal, to further enhance performance. Furthermore, due to drone regulations, the real-world demonstration of Hestia is conducted indoors using an indoor GPS system (e.g., HTC Lighthouse base stations). Drone policies vary across countries, and obtaining outdoor flight approvals can take up to a year in our region. Additionally, outdoor trials require significant funding, such as renting a safe test site measuring approximately 100 meters by 100 meters. As a future step, we plan to test the system with a larger customized drone in an outdoor private area to further validate its performance. Another future step is to extend Hestia to a multi-agent setting for large-scale outdoor scanning (e.g., city-scale) under power-constrained scenarios.

In addition to the above limitations, we hope that Hestia will not be misused for other types of next-best-view (NBV) tasks. In this study, we found that a greedy-like training scheme can effectively mitigate spurious correlations and is well-suited to our problem definition (see Sec. G, Sec. 3, and Sec. 5). However, the next-best-view problem is a broad research topic with varying objectives. This finding may not generalize to other NBV tasks, such as next-best-view for object tracking or next-best-view for human aesthetics, where long-term planning is more critical.

Also, although our quantitative and qualitative results (see Sec. 5 and Sec. C) demonstrate a nearly comprehensive point cloud reconstruction, we hope that Hestia will not be misused as a perfect next-best-view planner for 3D reconstruction. There are still some failure cases of Hestia (see Fig. 6). Hestia may occasionally fail to capture finer 3D structures, such as the window frames of the first row house shown in Fig. 6. It may also fail to reconstruct highly self-occluded parts, such as the pillar of the second row house. In addition, Hestia sometimes struggles to capture bottom-up views that require extreme vertical viewing angles, for example, the Lego man’s right hand and the underside of the pillar. Moreover, it may struggle to reconstruct shapes with fine details over coarse surfaces, such as tiny parts of the broccoli and anise. Adopting a multi-resolution grid structure or integrating octree-based methods to enhance the voxel grid resolution could be a potential future step to mitigate these issues.

Acknowledgments

If a paper is accepted, the final camera-ready version will (and probably should) include acknowledgments. All acknowledgments go at the end of the paper, including thanks to reviewers who gave useful comments, to colleagues who contributed to the ideas, and to funding agencies and corporate sponsors that provided financial support.

References

- [1] S. Agarwal, Y. Furukawa, N. Snavely, I. Simon, B. Curless, S. M. Seitz, and R. Szeliski. Building rome in a day. *Communications of the ACM*, 54(10):105–112, 2011.
- [2] H. Jiang, H. Liu, P. Tan, G. Zhang, and H. Bao. 3d reconstruction of dynamic scenes with multiple handheld cameras. In *Computer Vision–ECCV 2012: 12th European Conference on Computer Vision, Florence, Italy, October 7–13, 2012, Proceedings, Part II 12*, pages 601–615. Springer, 2012.
- [3] H. Kim and A. Hilton. 3d scene reconstruction from multiple spherical stereo pairs. *International journal of computer vision*, 104:94–116, 2013.
- [4] M. Nießner, M. Zollhöfer, S. Izadi, and M. Stamminger. Real-time 3d reconstruction at scale using voxel hashing. *ACM Transactions on Graphics (ToG)*, 32(6):1–11, 2013.
- [5] J. Xie, R. Girshick, and A. Farhadi. Deep3d: Fully automatic 2d-to-3d video conversion with deep convolutional neural networks. In *Computer Vision–ECCV 2016: 14th European Conference, Amsterdam, The Netherlands, October 11–14, 2016, Proceedings, Part IV 14*, pages 842–857. Springer, 2016.
- [6] J. L. Schönberger and J.-M. Frahm. Structure-from-motion revisited. In *Conference on Computer Vision and Pattern Recognition (CVPR)*, 2016.
- [7] Y. Yao, Z. Luo, S. Li, T. Fang, and L. Quan. Mvsnet: Depth inference for unstructured multi-view stereo. In *Proceedings of the European conference on computer vision (ECCV)*, pages 767–783, 2018.
- [8] H. Xie, H. Yao, X. Sun, S. Zhou, and S. Zhang. Pix2vox: Context-aware 3d reconstruction from single and multi-view images. In *Proceedings of the IEEE/CVF international conference on computer vision*, pages 2690–2698, 2019.
- [9] Z. Murez, T. Van As, J. Bartolozzi, A. Sinha, V. Badrinarayanan, and A. Rabinovich. Atlas: End-to-end 3d scene reconstruction from posed images. In *Computer Vision–ECCV 2020: 16th European Conference, Glasgow, UK, August 23–28, 2020, Proceedings, Part VII 16*, pages 414–431. Springer, 2020.
- [10] D. Wang, X. Cui, X. Chen, Z. Zou, T. Shi, S. Salcudean, Z. J. Wang, and R. Ward. Multi-view 3d reconstruction with transformers. In *Proceedings of the IEEE/CVF international conference on computer vision*, pages 5722–5731, 2021.
- [11] M. Sayed, J. Gibson, J. Watson, V. Prisacariu, M. Firman, and C. Godard. Simplerecon: 3d reconstruction without 3d convolutions. In *European Conference on Computer Vision*, pages 1–19. Springer, 2022.
- [12] H. Xu, J. Zhang, J. Cai, H. Rezatofighi, F. Yu, D. Tao, and A. Geiger. Unifying flow, stereo and depth estimation. *IEEE Transactions on Pattern Analysis and Machine Intelligence*, 2023.
- [13] S. Wang, V. Leroy, Y. Cabon, B. Chidlovskii, and J. Revaud. Dust3r: Geometric 3d vision made easy. In *Proceedings of the IEEE/CVF Conference on Computer Vision and Pattern Recognition*, pages 20697–20709, 2024.

- [14] B. P. Duisterhof, L. Zust, P. Weinzaepfel, V. Leroy, Y. Cabon, and J. Revaud. Mast3r-sfm: a fully-integrated solution for unconstrained structure-from-motion. *CoRR*, 2024.
- [15] L. Pan, D. Barath, M. Pollefeys, and J. L. Schönberger. Global Structure-from-Motion Revisited. In *European Conference on Computer Vision (ECCV)*, 2024.
- [16] B. Mildenhall, P. P. Srinivasan, M. Tancik, J. T. Barron, R. Ramamoorthi, and R. Ng. Nerf: Representing scenes as neural radiance fields for view synthesis. In *ECCV*, 2020.
- [17] A. Yu, V. Ye, M. Tancik, and A. Kanazawa. pixelnerf: Neural radiance fields from one or few images. In *Proceedings of the IEEE/CVF conference on computer vision and pattern recognition*, pages 4578–4587, 2021.
- [18] S. Fridovich-Keil, A. Yu, M. Tancik, Q. Chen, B. Recht, and A. Kanazawa. Plenoxels: Radiance fields without neural networks. In *CVPR*, 2022.
- [19] A. Chen, Z. Xu, A. Geiger, J. Yu, and H. Su. Tensorf: Tensorial radiance fields. In *European conference on computer vision*, pages 333–350. Springer, 2022.
- [20] T. Müller, A. Evans, C. Schied, and A. Keller. Instant neural graphics primitives with a multiresolution hash encoding. *ACM Trans. Graph.*, 41(4):102:1–102:15, July 2022. doi: 10.1145/3528223.3530127. URL <https://doi.org/10.1145/3528223.3530127>.
- [21] S. Sabour, S. Vora, D. Duckworth, I. Krasin, D. J. Fleet, and A. Tagliasacchi. Robustnerf: Ignoring distractors with robust losses. In *Proceedings of the IEEE/CVF Conference on Computer Vision and Pattern Recognition*, pages 20626–20636, 2023.
- [22] B. Kerbl, G. Kopanas, T. Leimkühler, and G. Drettakis. 3d gaussian splatting for real-time radiance field rendering. *ACM Trans. Graph.*, 42(4):139–1, 2023.
- [23] S. Zheng, B. Zhou, R. Shao, B. Liu, S. Zhang, L. Nie, and Y. Liu. Gps-gaussian: Generalizable pixel-wise 3d gaussian splatting for real-time human novel view synthesis. In *Proceedings of the IEEE/CVF Conference on Computer Vision and Pattern Recognition (CVPR)*, 2024.
- [24] K. Zhang, S. Bi, H. Tan, Y. Xiangli, N. Zhao, K. Sunkavalli, and Z. Xu. Gs-lrm: Large reconstruction model for 3d gaussian splatting. *European Conference on Computer Vision*, 2024.
- [25] W. Ren, Z. Zhu, B. Sun, J. Chen, M. Pollefeys, and S. Peng. Nerf on-the-go: Exploiting uncertainty for distractor-free nerfs in the wild. In *IEEE/CVF Conference on Computer Vision and Pattern Recognition (CVPR)*, 2024.
- [26] D. Charatan, S. L. Li, A. Tagliasacchi, and V. Sitzmann. pixelsplat: 3d gaussian splats from image pairs for scalable generalizable 3d reconstruction. In *Proceedings of the IEEE/CVF Conference on Computer Vision and Pattern Recognition*, pages 19457–19467, 2024.
- [27] S. Sabour, L. Goli, G. Kopanas, M. Matthews, D. Lagun, L. Guibas, A. Jacobson, D. J. Fleet, and A. Tagliasacchi. Spotlessplats: Ignoring distractors in 3d gaussian splatting. *arXiv preprint arXiv:2406.20055*, 2024.
- [28] J. Flynn, M. Broxton, L. Murmann, L. Chai, M. DuVall, C. Godard, K. Heal, S. Kaza, S. Lombardi, X. Luo, et al. Quark: Real-time, high-resolution, and general neural view synthesis. *ACM Transactions on Graphics (TOG)*, 43(6):1–20, 2024.
- [29] C. Ziwen, H. Tan, K. Zhang, S. Bi, F. Luan, Y. Hong, L. Fuxin, and Z. Xu. Long-lrm: Long-sequence large reconstruction model for wide-coverage gaussian splats. *arXiv preprint 2410.12781*, 2024.

- [30] Y. Chen, H. Xu, C. Zheng, B. Zhuang, M. Pollefeys, A. Geiger, T.-J. Cham, and J. Cai. Mvs-plat: Efficient 3d gaussian splatting from sparse multi-view images. In *European Conference on Computer Vision*, pages 370–386. Springer, 2025.
- [31] M. Wallingford, A. Bhattad, A. Kusupati, V. Ramanujan, M. Deitke, A. Kembhavi, R. Motlaghi, W.-C. Ma, and A. Farhadi. From an image to a scene: Learning to imagine the world from a million 360° videos. In *The Thirty-eighth Annual Conference on Neural Information Processing Systems*.
- [32] T. Yu, Z. Zheng, K. Guo, P. Liu, Q. Dai, and Y. Liu. Function4d: Real-time human volumetric capture from very sparse consumer rgbd sensors. In *IEEE Conference on Computer Vision and Pattern Recognition (CVPR2021)*, June 2021.
- [33] R. Jensen, A. Dahl, G. Vogiatzis, E. Tola, and H. Aanæs. Large scale multi-view stereopsis evaluation. In *Proceedings of the IEEE conference on computer vision and pattern recognition*, pages 406–413, 2014.
- [34] T. Zhou, R. Tucker, J. Flynn, G. Fyffe, and N. Snavely. Stereo magnification: Learning view synthesis using multiplane images. *arXiv preprint arXiv:1805.09817*, 2018.
- [35] A. Liu, R. Tucker, V. Jampani, A. Makadia, N. Snavely, and A. Kanazawa. Infinite nature: Perpetual view generation of natural scenes from a single image. In *Proceedings of the IEEE/CVF International Conference on Computer Vision*, pages 14458–14467, 2021.
- [36] L. Xu, V. Agrawal, W. Laney, T. Garcia, A. Bansal, C. Kim, S. Rota Bulò, L. Porzi, P. Kotschieder, A. Božič, et al. Vr-nerf: High-fidelity virtualized walkable spaces. In *SIG-GRAPH Asia 2023 Conference Papers*, pages 1–12, 2023.
- [37] M. Broxton, J. Flynn, R. Overbeck, D. Erickson, P. Hedman, M. DuVall, J. Dourgarian, J. Busch, M. Whalen, and P. Debevec. Immersive light field video with a layered mesh representation. 39(4):86:1–86:15, 2020.
- [38] K.-E. Lin, L. Xiao, F. Liu, G. Yang, and R. Ramamoorthi. Deep 3d mask volume for view synthesis of dynamic scenes. In *Proceedings of the IEEE/CVF International Conference on Computer Vision*, pages 1749–1758, 2021.
- [39] J. S. Yoon, K. Kim, O. Gallo, H. S. Park, and J. Kautz. Novel view synthesis of dynamic scenes with globally coherent depths from a monocular camera. In *Proceedings of the IEEE/CVF Conference on Computer Vision and Pattern Recognition*, pages 5336–5345, 2020.
- [40] T. Li, M. Slavcheva, M. Zollhoefer, S. Green, C. Lassner, C. Kim, T. Schmidt, S. Lovegrove, M. Goesele, R. Newcombe, et al. Neural 3d video synthesis from multi-view video. In *Proceedings of the IEEE/CVF Conference on Computer Vision and Pattern Recognition*, pages 5521–5531, 2022.
- [41] C.-Y. Lu, P. Zhou, A. Xing, C. Pokhariya, A. Dey, I. N. Shah, R. Mavidipalli, D. Hu, A. I. Comport, K. Chen, et al. Diva-360: The dynamic visual dataset for immersive neural fields. In *Proceedings of the IEEE/CVF Conference on Computer Vision and Pattern Recognition*, pages 22466–22476, 2024.
- [42] S. Peng, Y. Zhang, Y. Xu, Q. Wang, Q. Shuai, H. Bao, and X. Zhou. Neural body: Implicit neural representations with structured latent codes for novel view synthesis of dynamic humans. In *Proceedings of the IEEE/CVF Conference on Computer Vision and Pattern Recognition*, pages 9054–9063, 2021.
- [43] X. Chen, Q. Li, T. Wang, T. Xue, and J. Pang. Gennbv: Generalizable next-best-view policy for active 3d reconstruction. In *Proceedings of the IEEE/CVF Conference on Computer Vision and Pattern Recognition*, pages 16436–16445, 2024.

- [44] R. Monica and J. Aleotti. Contour-based next-best view planning from point cloud segmentation of unknown objects. *Autonomous Robots*, 42:443–458, 2018.
- [45] H. Zha, K. Morooka, and T. Hasegawa. Next best viewpoint (nbv) planning for active object modeling based on a learning-by-showing approach. In *Computer Vision—ACCV’98: Third Asian Conference on Computer Vision Hong Kong, China, January 8–10, 1998 Proceedings, Volume II 3*, pages 185–192. Springer, 1997.
- [46] L. Liu, X. Xia, H. Sun, Q. Shen, J. Xu, B. Chen, H. Huang, and K. Xu. Object-aware guidance for autonomous scene reconstruction. *ACM Transactions on Graphics (TOG)*, 37(4):1–12, 2018.
- [47] G. Hardouin, F. Morbidi, J. Moras, J. Marzat, and E. M. Mouaddib. Surface-driven next-best-view planning for exploration of large-scale 3d environments. *IFAC-PapersOnLine*, 53(2): 15501–15507, 2020.
- [48] G. Hardouin, J. Moras, F. Morbidi, J. Marzat, and E. M. Mouaddib. Next-best-view planning for surface reconstruction of large-scale 3d environments with multiple uavs. In *2020 IEEE/RSJ International Conference on Intelligent Robots and Systems (IROS)*, pages 1567–1574. IEEE, 2020.
- [49] K. Lin and B. Yi. Active view planning for radiance fields. In *Robotics Science and Systems*, 2022.
- [50] X. Pan, Z. Lai, S. Song, and G. Huang. Activenerf: Learning where to see with uncertainty estimation. In *European Conference on Computer Vision*, pages 230–246. Springer, 2022.
- [51] S. Lee, L. Chen, J. Wang, A. Liniger, S. Kumar, and F. Yu. Uncertainty guided policy for active robotic 3d reconstruction using neural radiance fields. *IEEE Robotics and Automation Letters*, 7(4):12070–12077, 2022.
- [52] H. Zhan, J. Zheng, Y. Xu, I. Reid, and H. Rezatofighi. Activermap: Radiance field for active mapping and planning. *arXiv preprint arXiv:2211.12656*, 2022.
- [53] L. Jin, X. Chen, J. Rückin, and M. Popović. Neu-nbv: Next best view planning using uncertainty estimation in image-based neural rendering. In *2023 IEEE/RSJ International Conference on Intelligent Robots and Systems (IROS)*, pages 11305–11312. IEEE, 2023.
- [54] N. Sünderhauf, J. Abou-Chakra, and D. Miller. Density-aware nerf ensembles: Quantifying predictive uncertainty in neural radiance fields. In *2023 IEEE International Conference on Robotics and Automation (ICRA)*, pages 9370–9376. IEEE, 2023.
- [55] D. Peralta, J. Casimiro, A. M. Nilles, J. A. Aguilar, R. Atienza, and R. Cajote. Next-best view policy for 3d reconstruction. *arXiv preprint arXiv:2008.12664*, 2020.
- [56] Y. Ran, J. Zeng, S. He, J. Chen, L. Li, Y. Chen, G. Lee, and Q. Ye. Neurar: Neural uncertainty for autonomous 3d reconstruction with implicit neural representations. *IEEE Robotics and Automation Letters*, 8(2):1125–1132, 2023.
- [57] A. Guédon, T. Monnier, P. Monasse, and V. Lepetit. Macarons: Mapping and coverage anticipation with rgb online self-supervision. In *Proceedings of the IEEE/CVF Conference on Computer Vision and Pattern Recognition*, pages 940–951, 2023.
- [58] W. Jiang, B. Lei, and K. Daniilidis. Fisherrf: Active view selection and uncertainty quantification for radiance fields using fisher information. *arXiv preprint arXiv:2311.17874*, 2023.
- [59] A. Boneh and M. Hofri. The coupon-collector problem revisited—a survey of engineering problems and computational methods. *Stochastic Models*, 13(1):39–66, 1997.

- [60] M. Deitke, D. Schwenk, J. Salvador, L. Weihs, O. Michel, E. VanderBilt, L. Schmidt, K. Ehsani, A. Kembhavi, and A. Farhadi. Objaverse: A universe of annotated 3d objects. In *Proceedings of the IEEE/CVF Conference on Computer Vision and Pattern Recognition (CVPR)*, pages 13142–13153, June 2023.
- [61] M. Deitke, R. Liu, M. Wallingford, H. Ngo, O. Michel, A. Kusupati, A. Fan, C. Laforte, V. Voleti, S. Y. Gadre, et al. Objaverse-xl: A universe of 10m+ 3d objects. *Advances in Neural Information Processing Systems*, 36, 2024.
- [62] A. C. INTERPRETATION. Spurious correlation: A causal interpretation herbert a. simon. *Causal Models in the Social Sciences*, page 5, 1971.
- [63] Y. Kim, S. Mo, M. Kim, K. Lee, J. Lee, and J. Shin. Discovering and mitigating visual biases through keyword explanation. In *Proceedings of the IEEE/CVF Conference on Computer Vision and Pattern Recognition*, pages 11082–11092, 2024.
- [64] J. Tang, J. Ren, H. Zhou, Z. Liu, and G. Zeng. Dreamgaussian: Generative gaussian splatting for efficient 3d content creation. *arXiv preprint arXiv:2309.16653*, 2023.
- [65] A. Nichol, H. Jun, P. Dhariwal, P. Mishkin, and M. Chen. Point-e: A system for generating 3d point clouds from complex prompts. *arXiv preprint arXiv:2212.08751*, 2022.
- [66] J. J. Park, P. Florence, J. Straub, R. Newcombe, and S. Lovegrove. Deepsdf: Learning continuous signed distance functions for shape representation. In *Proceedings of the IEEE/CVF conference on computer vision and pattern recognition*, pages 165–174, 2019.
- [67] Z.-X. Zou, Z. Yu, Y.-C. Guo, Y. Li, D. Liang, Y.-P. Cao, and S.-H. Zhang. Triplane meets gaussian splatting: Fast and generalizable single-view 3d reconstruction with transformers. In *Proceedings of the IEEE/CVF Conference on Computer Vision and Pattern Recognition*, pages 10324–10335, 2024.
- [68] N. Müller, A. Simonelli, L. Porzi, S. R. Bulò, M. Nießner, and P. Kotschieder. Autorf: Learning 3d object radiance fields from single view observations. In *Proceedings of the IEEE/CVF Conference on Computer Vision and Pattern Recognition*, pages 3971–3980, 2022.
- [69] Y.-L. Liu, C. Gao, A. Meuleman, H.-Y. Tseng, A. Saraf, C. Kim, Y.-Y. Chuang, J. Kopf, and J.-B. Huang. Robust dynamic radiance fields. In *Proceedings of the IEEE/CVF Conference on Computer Vision and Pattern Recognition*, pages 13–23, 2023.
- [70] Q. Wang, Z. Wang, K. Genova, P. Srinivasan, H. Zhou, J. T. Barron, R. Martin-Brualla, N. Snavely, and T. Funkhouser. Ibrnet: Learning multi-view image-based rendering. In *CVPR*, 2021.
- [71] H. Lin, S. Peng, Z. Xu, Y. Yan, Q. Shuai, H. Bao, and X. Zhou. Efficient neural radiance fields for interactive free-viewpoint video. In *SIGGRAPH Asia Conference Proceedings*, 2022.
- [72] A. Chen, Z. Xu, F. Zhao, X. Zhang, F. Xiang, J. Yu, and H. Su. Mvsnerf: Fast generalizable radiance field reconstruction from multi-view stereo. In *Proceedings of the IEEE/CVF International Conference on Computer Vision*, pages 14124–14133, 2021.
- [73] H. Gao, R. Li, S. Tulsiani, B. Russell, and A. Kanazawa. Monocular dynamic view synthesis: A reality check. *Advances in Neural Information Processing Systems*, 35:33768–33780, 2022.
- [74] K. Park, U. Sinha, J. T. Barron, S. Bouaziz, D. B. Goldman, S. M. Seitz, and R. Martin-Brualla. Nerfies: Deformable neural radiance fields. *ICCV*, 2021.
- [75] K. Park, U. Sinha, P. Hedman, J. T. Barron, S. Bouaziz, D. B. Goldman, R. Martin-Brualla, and S. M. Seitz. Hypernerf: A higher-dimensional representation for topologically varying neural radiance fields. *ACM Trans. Graph.*, 40(6), dec 2021.

- [76] L. Ling, Y. Sheng, Z. Tu, W. Zhao, C. Xin, K. Wan, L. Yu, Q. Guo, Z. Yu, Y. Lu, et al. D13dv-10k: A large-scale scene dataset for deep learning-based 3d vision. In *Proceedings of the IEEE/CVF Conference on Computer Vision and Pattern Recognition*, pages 22160–22169, 2024.
- [77] C. Lu, F. Yin, X. Chen, W. Liu, T. Chen, G. Yu, and J. Fan. A large-scale outdoor multi-modal dataset and benchmark for novel view synthesis and implicit scene reconstruction. In *Proceedings of the IEEE/CVF International Conference on Computer Vision*, pages 7557–7567, 2023.
- [78] K. Grauman, A. Westbury, L. Torresani, K. Kitani, J. Malik, T. Afouras, K. Ashutosh, V. Baiyya, S. Bansal, B. Boote, et al. Ego-exo4d: Understanding skilled human activity from first-and third-person perspectives. In *Proceedings of the IEEE/CVF Conference on Computer Vision and Pattern Recognition*, pages 19383–19400, 2024.
- [79] H. Chen, Y. Hou, C. Qu, I. Testini, X. Hong, and J. Jiao. 360+x: A panoptic multi-modal scene understanding dataset. In *Proceedings of the IEEE/CVF Conference on Computer Vision and Pattern Recognition*, 2024.
- [80] L. Li, Z. Shen, Z. Wang, L. Shen, and P. Tan. Streaming radiance fields for 3d video synthesis. *Advances in Neural Information Processing Systems*, 35:13485–13498, 2022.
- [81] J. Shen, A. Ruiz, A. Agudo, and F. Moreno-Noguer. Stochastic neural radiance fields: Quantifying uncertainty in implicit 3d representations. In *2021 International Conference on 3D Vision (3DV)*, pages 972–981. IEEE, 2021.
- [82] R. Martin-Brualla, N. Radwan, M. S. Sajjadi, J. T. Barron, A. Dosovitskiy, and D. Duckworth. Nerf in the wild: Neural radiance fields for unconstrained photo collections. In *Proceedings of the IEEE/CVF conference on computer vision and pattern recognition*, pages 7210–7219, 2021.
- [83] S. Umeyama. Least-squares estimation of transformation parameters between two point patterns. *IEEE Transactions on Pattern Analysis & Machine Intelligence*, 13(04):376–380, 1991.
- [84] M. Mittal, C. Yu, Q. Yu, J. Liu, N. Rudin, D. Hoeller, J. L. Yuan, R. Singh, Y. Guo, H. Mazhar, A. Mandlekar, B. Babich, G. State, M. Hutter, and A. Garg. Orbit: A unified simulation framework for interactive robot learning environments. *IEEE Robotics and Automation Letters*, 8(6):3740–3747, 2023. doi:10.1109/LRA.2023.3270034.
- [85] T. Wu, J. Zhang, X. Fu, Y. Wang, J. Ren, L. Pan, W. Wu, L. Yang, J. Wang, C. Qian, et al. Omniobject3d: Large-vocabulary 3d object dataset for realistic perception, reconstruction and generation. In *Proceedings of the IEEE/CVF Conference on Computer Vision and Pattern Recognition*, pages 803–814, 2023.
- [86] Q.-Y. Zhou, J. Park, and V. Koltun. Open3d: A modern library for 3d data processing. *arXiv preprint arXiv:1801.09847*, 2018.
- [87] H. Abdi and L. J. Williams. Principal component analysis. *Wiley interdisciplinary reviews: computational statistics*, 2(4):433–459, 2010.
- [88] J. MacQueen et al. Some methods for classification and analysis of multivariate observations. In *Proceedings of the fifth Berkeley symposium on mathematical statistics and probability*, volume 1, pages 281–297. Oakland, CA, USA, 1967.
- [89] J. Schulman, F. Wolski, P. Dhariwal, A. Radford, and O. Klimov. Proximal policy optimization algorithms. *arXiv preprint arXiv:1707.06347*, 2017.
- [90] A. Raffin, A. Hill, A. Gleave, A. Kanervisto, M. Ernestus, and N. Dormann. Stable-baselines3: Reliable reinforcement learning implementations. *Journal of Machine Learning Research*, 22(268):1–8, 2021. URL <http://jmlr.org/papers/v22/20-1364.html>.

Appendix

In this appendix, we present the theoretical grounding for treating voxels as cubes in Sec. A, additional quantitative results in Sec. B, further qualitative results in Sec. C, real-world demonstration results in Sec. D, details of the reward design in Sec. E, the novelty of the proposed components in Sec. F, the impact of spurious correlations in Sec. G, the ablation study in Sec. H, dataset details and preparation in Sec. I, the real-world system setup and associated costs in Sec. J, and training and testing details in Sec. K. We hope readers understand that the main paper is limited to 8 pages, and therefore, we have included 11 additional sections in the appendix. We have made every effort to link the main paper with the appendix to improve the reading experience.

A Theoretical Grounding

Although treating a voxel as a cube rather than a point straightforwardly avoids overlooking surface geometry, we formalize the benefit through the following constrained example from a theoretical perspective. Consider a scene composed of k unit cubes and a 1-ray camera that emits a single ray per sample, where each ray is assumed to intersect one of the cubes in the scene. We contrast two sampling rules:

- **Scenario 1 (voxel as a point).** Continue sampling until every cube has been intersected by at least one ray.
- **Scenario 2 (voxel as a cube).** Continue sampling until every face of every cube has been intersected by at least one ray.

Our goal is to compare the expected face visibility achieved after the scenarios terminate. Hitting each of the k cubes at least once can be treated as a classical coupon-collector problem [59], whose expectation is:

$$k \left(1 + \frac{1}{2} + \dots + \frac{1}{k} \right) \approx k \ln k. \tag{A1}$$

Every ray that hits a cube intersects one of its six faces uniformly at random, so each ray can be viewed as a draw from:

$$N = 6k \tag{A2}$$

distinct faces. After n rays, the probability that a specific face is still unseen is:

$$\left(1 - \frac{1}{6k} \right)^n \approx e^{-\frac{n}{6k}}, \quad 6k \gg 1. \tag{A3}$$

Hence, through Eq. A1 and Eq. A3, we know that after Scenario 1 stops, the ratio of the expected non-visible faces is:

$$e^{-\frac{k \ln k}{6k}} = k^{-\frac{1}{6}}. \tag{A4}$$

If $k = 8000$, roughly 22.3% of the faces remain unseen for Scenario 1, while Scenario 2 can cover all the faces. This theoretical result further motivates treating voxels as cubes rather than points when designing next-best-view policies.

B Benchmark Details

In this section, we present the detailed coverage ratio (CR), Chamfer Distance (CD), and area under the coverage ratio curve (AUC) from Tab. 1, broken down by each object position setting in Tab. A1, A2, and A3. Both Hestia and Hestia-H3K outperform other baselines across all object position settings in the OmniObject3D [85], Objaverse [60], and Houses3K [55] test splits. Moreover, Hestia and Hestia-H3K are the only methods that demonstrate robust performance across all object position settings on all three datasets, with less than a 1% coverage ratio difference across different object configurations. Interestingly, Hestia slightly outperforms Hestia-H3K in terms of Chamfer Distance when evaluated on in-distribution data (e.g., Houses3K), highlighting the benefit of using a more diverse training set.

Method	OmniObject3D Test				
	Object Center				
	(0, 0)	(4, 4)	(4, -4)	(-4, 4)	(-4, -4)
NeU-NBV [53]	88 / 24 / 83	73 / 51 / 70	75 / 75 / 70	72 / 53 / 69	76 / 38 / 71
ScanRL [55]	87 / 21 / 80	79 / 37 / 76	84 / 21 / 78	72 / 47 / 71	76 / 35 / 72
GenNBV [43]	92 / 12 / 88	92 / 14 / 86	91 / 15 / 83	94 / 10 / 89	94 / 9 / 88
GenNBV (Rep.) [43]	93 / 10 / 87	94 / 9 / 89	92 / 12 / 85	94 / 10 / 88	92 / 11 / 85
Hestia-H3K	97 / 5 / 94	97 / 5 / 92	96 / 7 / 92	96 / 5 / 92	96 / 6 / 93
Hestia	97 / 4 / 94	97 / 4 / 93	97 / 5 / 92	97 / 4 / 93	96 / 5 / 93

Table A1: **CR (%) / CD (cm) / AUC (%) comparison on the OmniObject3D test set.** Both Hestia and Hestia-H3K outperform other baselines and can achieve robust performance across different object positions.

Method	Objaverse Test				
	Object Center				
	(0, 0)	(4, 4)	(4, -4)	(-4, 4)	(-4, -4)
NeU-NBV [53]	88 / 20 / 83	76 / 41 / 74	77 / 31 / 72	77 / 41 / 74	78 / 31 / 72
ScanRL [55]	87 / 18 / 82	80 / 31 / 78	82 / 23 / 77	77 / 37 / 76	80 / 27 / 76
GenNBV [43]	94 / 11 / 89	90 / 15 / 85	89 / 17 / 82	93 / 12 / 89	91 / 13 / 86
GenNBV (Rep.) [43]	94 / 11 / 88	92 / 12 / 88	90 / 15 / 82	92 / 12 / 88	90 / 14 / 84
Hestia-H3K	96 / 8 / 93	95 / 8 / 91	95 / 9 / 90	96 / 9 / 93	95 / 8 / 90
Hestia	96 / 7 / 93	96 / 7 / 92	96 / 6 / 91	96 / 7 / 93	96 / 8 / 91

Table A2: **CR (%) / CD (cm) / AUC (%) comparison on the Objaverse test set.** Both Hestia and Hestia-H3K outperform other baselines and can achieve robust performance across different object positions.

Method	Houses3K Test				
	Object Center				
	(0, 0)	(4, 4)	(4, -4)	(-4, 4)	(-4, -4)
NeU-NBV [53]	85 / 26 / 80	73 / 52 / 71	81 / 30 / 77	72 / 53 / 70	80 / 32 / 76
ScanRL [55]	86 / 21 / 79	77 / 40 / 75	88 / 19 / 82	72 / 50 / 69	81 / 28 / 76
GenNBV [43]	94 / 10 / 89	90 / 18 / 83	91 / 16 / 84	94 / 12 / 89	93 / 12 / 89
GenNBV (Rep.) [43]	94 / 12 / 88	95 / 10 / 90	94 / 13 / 88	94 / 11 / 89	91 / 14 / 88
Hestia-H3K	98 / 6 / 96	98 / 6 / 96	97 / 8 / 95	97 / 7 / 96	97 / 7 / 95
Hestia	97 / 5 / 96	97 / 5 / 93	97 / 7 / 93	97 / 5 / 94	97 / 7 / 93

Table A3: **CR (%) / CD (cm) / AUC (%) comparison on the Houses3K test set.** Both Hestia and Hestia-H3K outperform other baselines and can achieve robust performance across different object positions.

C Qualitative Results

In this section, we present additional qualitative results for OmniObject3D [85], Objaverse [60], and Houses3K [55] in Fig. A1, Fig. A2, Fig. A3, and Fig. A4. Fig. A1 shows that Hestia’s viewpoints successfully reconstruct the point clouds of real-world scanned objects, while other baselines often miss parts and perform less robustly across various object shapes. Specifically, other baselines miss the teddy bear’s body, the model toy’s face or skirt, the starfish’s arms, the sofa’s front or bottom, the plant’s pot, the statue’s head or stand, the table’s surface, and the durian’s flesh. All these diverse missing parts are captured by Hestia. Fig. A2 shows that Hestia’s viewpoints robustly cover various object shapes, while other baselines often miss finer details or parts underneath. Specifically, other methods miss the wooden stand’s legs, the Lego man’s face or arms, the lamp’s lampshade or neck, the underside of the wooden log, the tree’s leaves, the stairway’s columns or walls, and the cac-



Figure A1: **Qualitative comparison on OmniObject3D [85].** Hestia’s viewpoints reconstruct the point clouds of real-world scanned objects accurately, while other baselines exhibit less robustness across various object shapes, often missing parts in the reconstructed point clouds.

tus’s hat or hands. In contrast, Hestia successfully captures all these diverse and challenging parts. Fig. A3 shows that Hestia’s viewpoints can effectively capture building-like structures, while other methods often miss features such as pillars, roof soffits, or windows. Fig. A4 shows that Hestia is the only method that achieves consistent performance across different object position settings. These visualization results validate that our proposed core components, including dataset choice, observation design, action space, reward calculation, and learning scheme, form a significant foundation for the tasks and thereby bring a non-marginal impact.

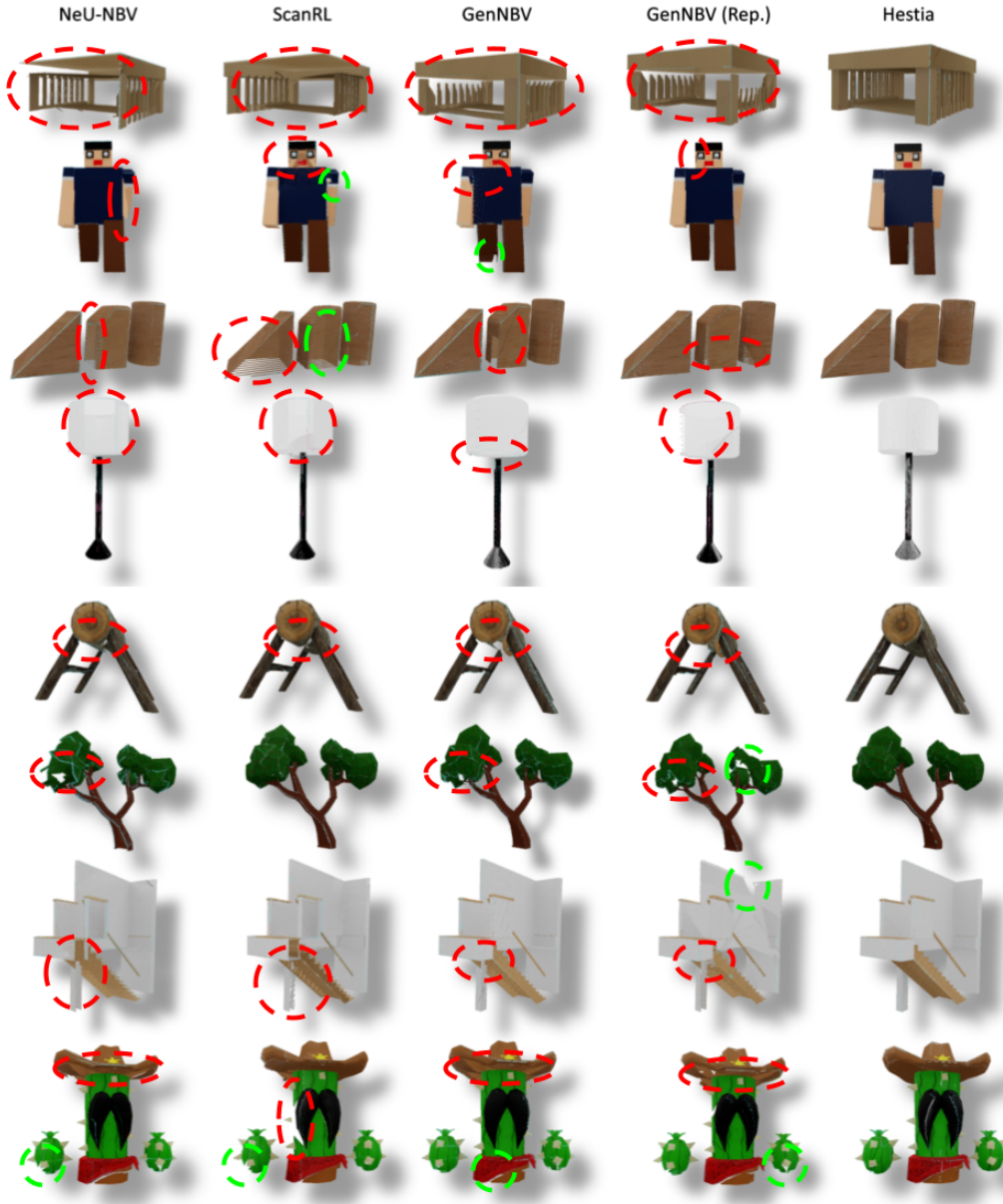


Figure A2: **Qualitative comparison on Objaverse [60].** Hestia's viewpoints successfully reconstruct diverse and complex object shapes, while other baselines exhibit less robustness, often missing self-occluded regions or parts that require bottom-up viewpoints.

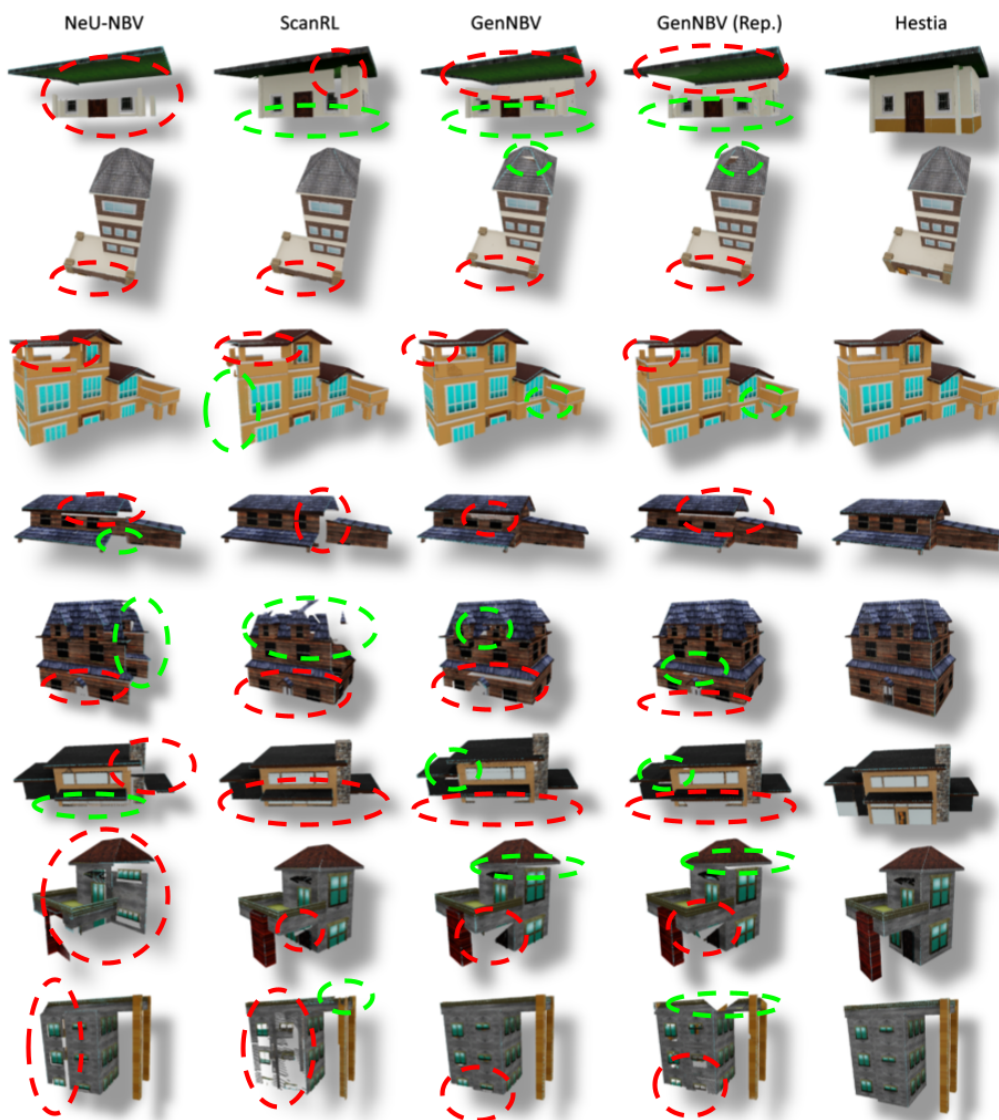


Figure A3: **Qualitative comparison on Houses3K [55]**. Compared to the baselines, the point clouds reconstructed from the depth maps collected by Hestia capture finer details, such as roof soffits, pillars, and windows, particularly in self-occluded areas.



Figure A4: **Qualitative comparison of objects at the four corners.** Hestia performs robustly across different object position settings, while other baselines fail to maintain consistent performance across positions.

D Real-World Results

In this section, we present real-world images captured using Hestia operating within the proposed data collection system. Fig. A5 demonstrates that Hestia performs well in real-world scenarios,

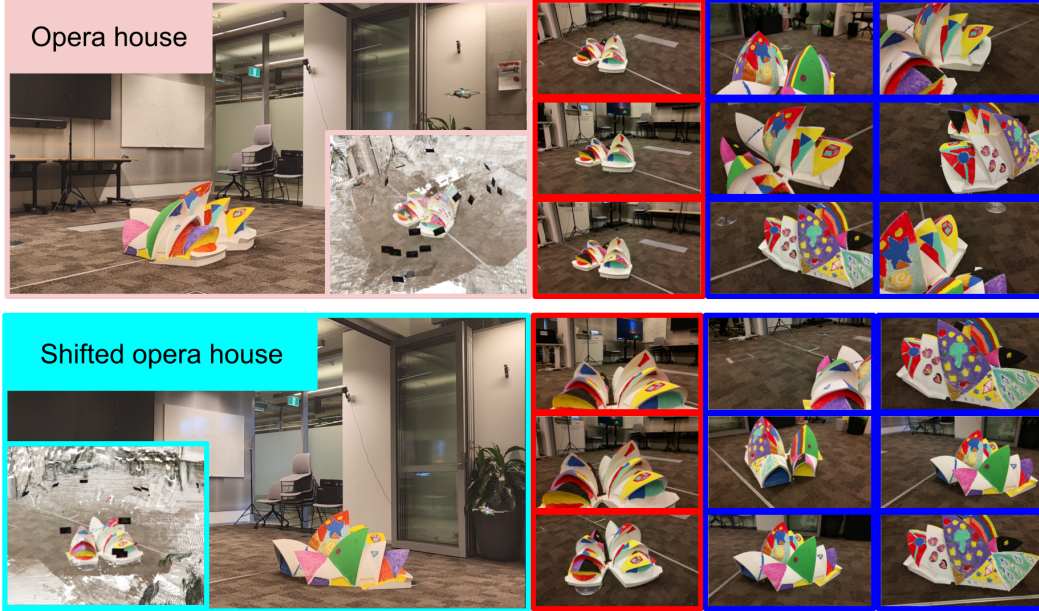


Figure A5: **Real-world demonstration of non-shifted and shifted scenes.** Hestia can operate in real-world scenarios with three initial viewpoints (red rectangles) and predict the next-best viewpoints for capture (blue rectangles for the first six views), even when the depth camera is unavailable. Point cloud reconstruction results are shown on the left, with black rectangles representing camera poses.

even when the depth camera is unavailable, for both shifted and non-shifted cases. Fig. A6 shows that Hestia robustly handles various real-world object shapes. These results demonstrate that Hestia surpasses prior works, which have not been validated in real-world environments. In addition, Hestia is suitable for use as a viewpoint predictor for real-world applications.

E Reward Design

In this section, we review the design of our reward function. The reward function in Hestia is formulated as

$$r_t = R(s_t, a_t) = r_{\text{coverage}}(s_t, a_t) + r_{\text{constraint}}(s_t, a_t). \quad (\text{A5})$$

To promote the exploration of previously unseen surfaces, we define the positive reward as

$$r_{\text{coverage}}(s_t, a_t) = \frac{\sum_{i=1}^N \sum_{j=1}^6 (F_t^{i,j} - F_{t-1}^{i,j}) \cdot M_{\text{col}}}{N \cdot 6} \cdot 0.3, \quad (\text{A6})$$

where $F_t^{i,j}$ and $F_{t-1}^{i,j}$ denote the visibility status of the j -th face of the i -th voxel at time t and $t - 1$, respectively. The variable $M_{\text{col}} \in \{0, 1\}$ acts as a collision indicator, set to 0 when a collision occurs, thereby nullifying any potential reward for unsafe actions. This reward is computed based on the increment in newly visible voxel faces at the current step. By focusing on the increment rather than the accumulated visibility, the agent is better able to associate rewards with the immediate effects of

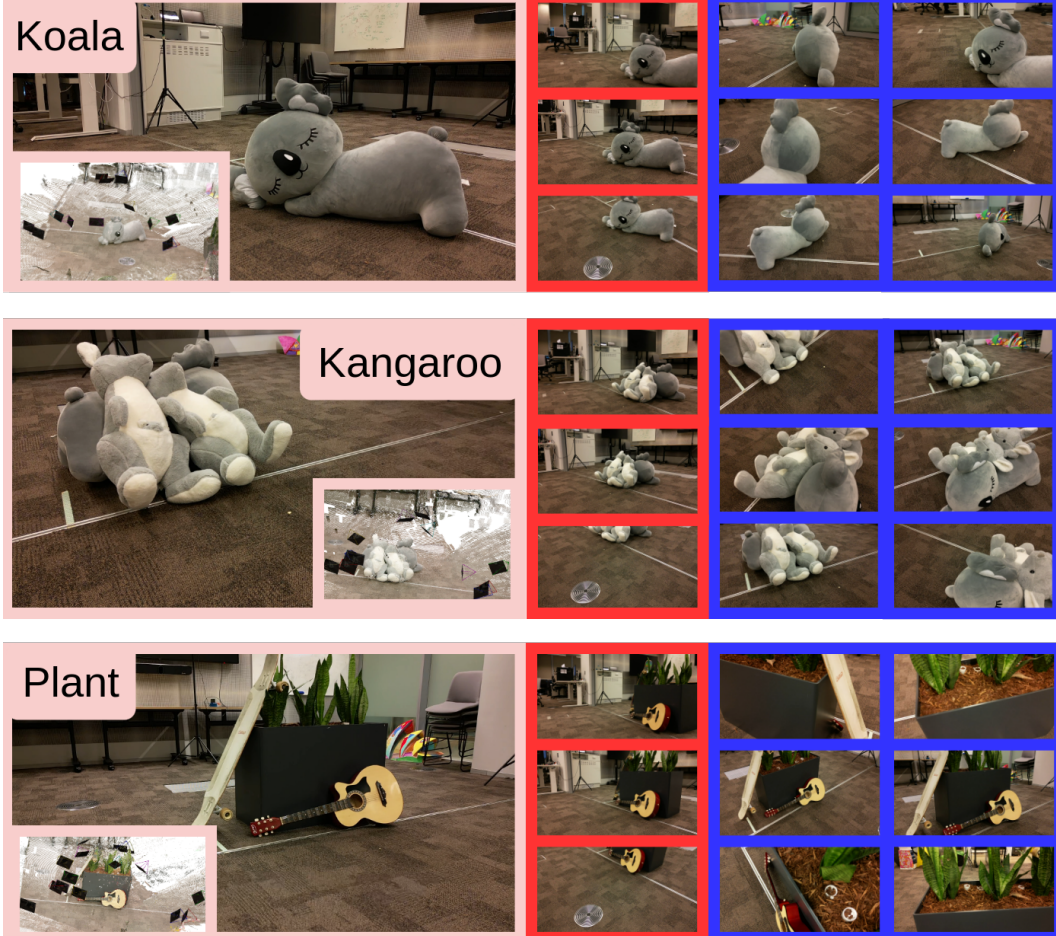


Figure A6: **Real-world demonstration of various scenes.** Hestia operates in real-world scenarios starting from three initial viewpoints (red rectangles) and predicts the next-best viewpoints for capture (blue rectangles for the first six views), even when the depth camera is unavailable. Point cloud reconstruction results are shown on the left, with black rectangles representing the camera poses.

its actions. To discourage unsafe or invalid decisions, we define a penalty as

$$r_{\text{constraint}}(s_t, a_t) = \begin{cases} -0.01, & \text{if } r_{\text{coverage}}(s_t, a_t) = 0, \\ & \text{or } a_t[2] > H_t, \\ & \text{or } a_t \in \text{non-free voxels}, \\ 0, & \text{otherwise.} \end{cases} \quad (\text{A7})$$

In particular, a negative reward is assigned if the agent fails to reveal any new faces, attempts to move above the maximum allowable flight height H_t , or selects a viewpoint located within non-free voxels. To ensure a balance between positive and negative rewards, the positive reward is scaled by a factor of 0.3. This weighting is based on the observation that the maximum face ratio is 1 and each episode ends after 50 steps. As a result, the total possible positive reward is approximately $0.3 \times 1 = 0.3$, which roughly aligns with the maximum overall value of the negative penalty $0.01 \times 50 = 0.5$. If the episode ends earlier, such as after 30 steps, this reward structure maintains a perfect balance.

F Novelty Justification

This section elaborates on the novelty of Hestia. Unlike prior approaches, Hestia systematically addresses the next-best-view task by introducing core components such as dataset selection, observation design, action space formulation, reward computation, and learning schemes. Together,

Method	No Cand. View	No Online Learn.	Voxel as Cube	Hier. Str.	Greedy	Div. Data.	Robust for Shift.	Real-World Demo.
Active3D [49]	X	X	–	X	–	X	–	X
NeRF-En [54]	X	X	–	X	–	X	–	X
ActiveNeRF [50]	X	X	–	X	–	X	–	X
NeurAR [56]	X	X	–	X	–	X	–	X
UnGuide [51]	X	X	–	X	–	X	–	✓
ActiveRMAP [52]	X	X	–	X	–	X	–	X
MACARONS [57]	X	X	–	X	–	–	–	X
NeU-NBV [53]	X	✓	–	X	–	X	X	X
ScanRL [55]	✓	✓	–	X	X	X	X	X
GenNBV [43]	✓	✓	X	X	X	X	X	X
Hestia	✓	✓	✓	✓	✓	✓	✓	✓

Table A4: **Comparison of learning-based next-best-view methods.** Compared to online learning methods, Hestia achieves real-time inference speed. Compared to generalizable methods, Hestia is the only one that performs robustly across different object position settings and demonstrates feasibility in real-world scenarios.

these elements form a comprehensive and unified foundation for the planner (see Sec. H). As shown in Tab. A4, compared to online-learning methods [49, 50, 51, 52, 54, 56, 57], Hestia avoids the need to sample candidate views or perform online optimization. This results in greater flexibility in viewpoint prediction and supports real-time inference. Additionally, in comparison to generalizable methods [43, 53, 55], Hestia is trained on a significantly larger and more diverse dataset, enabling it to generalize robustly to a wide variety of object shapes during testing. Hestia is also the only method that consistently performs well under different object configurations, as demonstrated in Tab. A1, Tab. A2, and Tab. A3. These advantages stem from the key innovations in our design, including treating voxels as cubes rather than points, employing a hierarchical structure to manage the complexity of the action space, and using a greedy learning scheme to mitigate spurious correlations.

G Spurious Correlation

In this section, we present the spurious correlation caused by future positive rewards in the task.

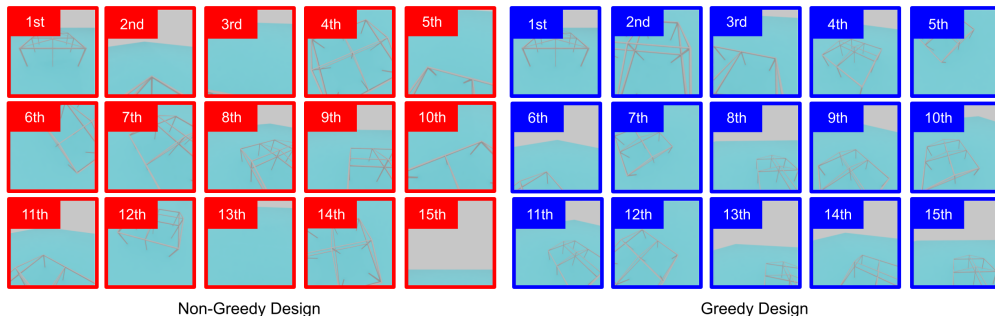


Figure A7: **Spurious correlation.** In this study, spurious correlation refers to the assignment of future positive rewards to current non-beneficial actions, resulting in suboptimal viewpoint predictions. For instance, the third, thirteenth, and fifteenth viewpoints are empty in the non-greedy design, while enabling the greedy design alleviates this issue.

Spurious correlation has been widely observed across various tasks [62, 63]. In our task, we find that using a large discount factor and future goal rewards can lead to false associations between current actions and their rewards. This creates an illusion for the RL agent that the current action is

beneficial, even when there is no information gain (e.g., empty views as shown in Fig. A7) resulting from the current action. Enabling the greedy design mitigates this issue as shown in Fig. A7.

H Ablation Study

This section validates that Hestia achieves the best performance when all proposed components are combined. We conduct an ablation study (see Tab. A5) on the three concepts of Hestia: using faces

	Face	Greedy	Hier.	Avg. CR \uparrow	Avg. CD \downarrow	#Pa.
				0.88	0.20	6.2M
Hestia	✓			0.90	0.17	6.2M
	✓	✓		0.95	0.09	6.2M
	✓	✓	✓	0.96	0.07	4.9M

Table A5: **Ablations.** Integrating the proposed ideas with the Objaverse [60, 61] dataset yields top performance with fewer parameters.

as observations, the greedy formulation with a small discount factor and no goal reward, and the hierarchical structure. For simplicity, we keep the input states consistent with Hestia, and for the non-hierarchical structure, we feed the encoded grid information into the policy model to predict 5-DoF viewpoints without feature interpolation. The results show that all these components are essential to improving the performance.

I Datasets

This section briefly introduces the three main datasets used in the Hestia benchmark: Houses3K [55], Objaverse [60, 61], and OmniObject3D [85].



Figure A8: **Sample data from Houses3K [55], Objaverse [60], and OmniObject3D [85].** Houses3K features building shapes with challenging self-occlusions, such as roof soffits. Objaverse includes a diverse range of object shapes. OmniObject3D contains high-quality real-world 3D scans.

I.1 Introduction to Datasets

Houses3K Dataset. Houses3K [55] is designed for next-best-view policy learning. The dataset contains 600 distinct buildings, each rendered with five texture variants, yielding a total of 3,000 FBX models. Many buildings feature challenging self-occlusions, such as roof soffits, that can be fully observed only from bottom-up viewpoints (see Fig. A8). However, because the dataset includes only a single cube-like object category (e.g., buildings), its diversity is limited, which may hinder the ability of next-best-view policies trained on Houses3K to generalize to other structures or everyday objects.

Objaverse Dataset. Objaverse [60] is one of the largest open 3D datasets, containing more than 800,000 shapes across at least 18 high-level categories, including furniture, vehicles, animals, and plants (see Fig. A8). Each category is further divided into several subcategories. The dataset’s scale and diversity make it particularly well suited for foundation model research, especially for 3D generative models. To the best of our knowledge, we are the first to introduce Objaverse for next-best-view policy learning. Its large-scale and diverse object coverage enables training next-best-view policies that perform robustly across a wide range of categories and shapes.

OmniObject3D Dataset. OmniObject3D [85] is a high-quality 3D object dataset collected through real-world scanning, consisting of approximately 6,000 objects across more than 190 categories (see Fig. A8). Unlike synthetic datasets, OmniObject3D captures real-world geometry and texture details using high-resolution 2D and 3D sensors. It provides accurate geometry and realistic material properties, making it commonly used for evaluating real-world transferability in vision tasks such as novel-view synthesis. In this paper, we introduce OmniObject3D for benchmark purposes.

I.2 Dataset Preparation

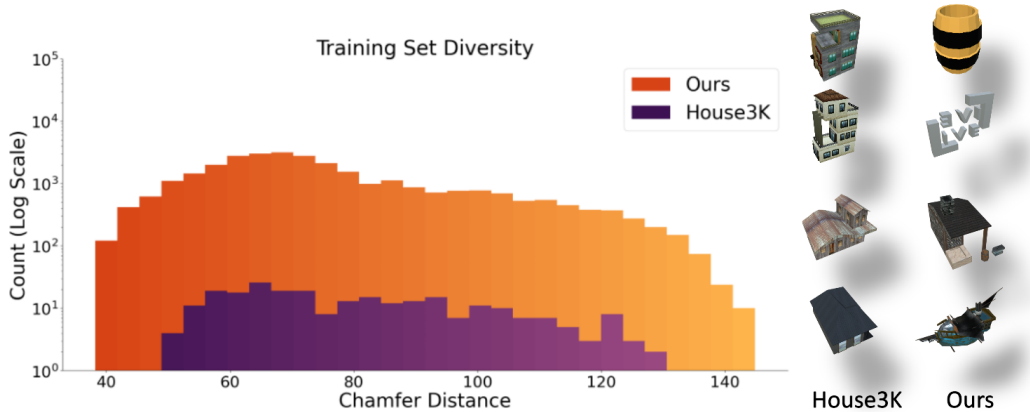


Figure A9: **More diverse and large-scale training set.** The chamfer distance measures the discrepancy between the point cloud of the training data and the sphere point cloud. The logarithmic scale of the count represents the number of shapes within each distance range. The right portion displays sample shapes with the same chamfer distance, shown side by side for each dataset. The wider chamfer distance range, higher number of shapes per chunk, and varied shape categories demonstrate that our training data, processed from Objaverse [60, 61], are more comprehensive and large-scale compared to House3K.

We propose using Objaverse [60, 61] as the training dataset to ensure a diverse range of shapes during training (see Fig. A9 and Fig. A10). To achieve this, we filter out large meshes and download the remaining mesh files from Objaverse [60, 61], resulting in a dataset comprising 120,000 shapes. For each shape, we generate the occupancy grid and point cloud using Open3D [86]. To remove invisible voxels and points, we perform a breadth-first search (BFS) starting from external free voxels, retaining only reachable occupancy voxels and points as the ground truth. The visible faces of each voxel are identified by examining the occupancy states of neighboring voxels. We apply

PCA [87] to reduce the point cloud to three components and use k-means clustering [88] to group the 120,000 shapes into 30,100 clusters. The cluster centers of 30,000 clusters are designated as training data, while the remaining cluster centers are used for testing. The same procedure is used to create 256 training samples and 100 test samples from the House3K dataset [55] for our benchmark. Our

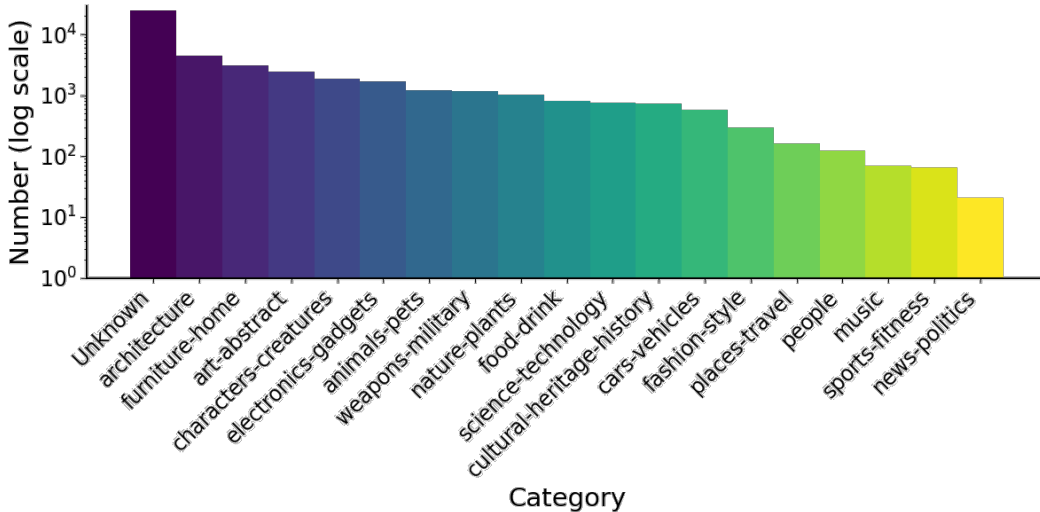


Figure A10: **Dataset distribution.** Our training dataset, processed from Objaverse [60, 61], includes a wide range of categories and is not limited to cubic-like shapes (e.g., buildings).

processed training set is two orders of magnitude larger than those used in previous studies [43, 53, 55] and includes at least 18 more categories than prior datasets [43, 55]. As for OmniObject3D [85], due to limited storage space, we randomly select one shape per category for evaluation, resulting in approximately 200 test samples.

J Real-World Data Collection System

This section includes the setup and pseudo code of the proposed real-world data collection system. By integrating Hestia into the proposed real-world data collection system, Hestia demonstrates its feasibility under practical scenarios, surpassing prior approaches.

J.1 Real-World System Setup

The environment size of our scenarios (e.g., an opera house) is approximately $2.6\text{ m} \times 2.6\text{ m} \times 2\text{ m}$. To prevent the drone from exceeding the HTC Lighthouse base station range, the maximum height H_t is restricted to 1.5 m. Additionally, in the nearest collision-free voxel module, voxels below 0.4m are marked as occupied to avoid potential counterforces between the floor and the drone’s quadrotor. In this system, we deploy the DJI Mini 3 Pro as the primary aircraft model.

We integrate the DJI Mobile SDK v5 to enable remote control and command transmission from the base station to the UAV. This software development kit provides developers with comprehensive control capabilities over the UAV. The SDK is embedded in an Android application package, where we develop a custom application capable of broadcasting aircraft data via the User Datagram Protocol (UDP) wireless network protocol. The broadcasted data is captured using a Raspberry Pi 4, which runs a ROS 2 node designed to receive UDP packets and convert them into ROS 2-compatible messages. On the same Raspberry Pi 4, we implement an adaptive trajectory planning technique. This method evaluates a pre-generated library of feasible offline trajectories, allowing the UAV to navigate autonomously by selecting the most appropriate path based on real-time conditions. Integrating these components ensures a reliable flow of data and commands, enabling efficient autonomous navigation for the UAV. We utilize the Crazyflie v2.1, a nano UAV equipped with a Lighthouse Po-

sitioning Deck, to achieve precise localization within the experimental environment. To integrate its capabilities with the primary aircraft, we remove the propellers and motors of the Crazyflie and securely mount it on top of the DJI Mini 3 Pro. This setup enables the Crazyflie to serve as a localization beacon, providing accurate positional data for the main UAV within the tracking range of the Lighthouse base stations. The positioning deck on the Crazyflie captures localization data using infrared signals from the Lighthouse system. This data is transmitted wirelessly via the Crazyradio 2.0 module, which connects to a base station. The base station, running the Crazyswarm 2.0 package on the ROS 2 framework, processes and publishes the localization data in real time. This setup facilitates autonomous navigation and precise positioning of the main UAV by continuously updating its coordinates within the experimental space.

To ensure reproducibility, our system is constructed entirely from publicly available, low-cost hardware, and we will release the accompanying code to support open research. The total cost of the additional components, including the Crazyflie v2.1 (approximately \$200), the Lighthouse Positioning Deck (around \$100), and the Crazyradio 2.0 module (about \$50), is approximately \$350. When combined with the DJI Mini 3 Pro, which costs around \$800, the total system cost remains significantly lower than that of conventional localization solutions. This cost-effective design, combined with open-source software such as ROS 2 and the Crazyswarm package, provides a reliable and accessible prototype for UAV-based data collection.

J.2 Real-World System Processes

Algorithm 1 *Main*

Require: A drone system $\mathcal{D} = \{\mathcal{D}_{gs}, \mathcal{D}_{pi}, \mathcal{D}_{ad}, \mathcal{D}_{ct}, \mathcal{D}_{drone}\}$, **where:**

\mathcal{D}_{gs} : Ground station
 \mathcal{D}_{pi} : Raspberry Pi
 \mathcal{D}_{ad} : Android phone
 \mathcal{D}_{ct} : Remote controller
 \mathcal{D}_{drone} : Drone

```

1:  $\mathcal{X} \leftarrow [x_1, x_2, x_3]$   $\triangleright$  Initial viewpoints
2: for  $x \in \mathcal{X}$  do
3:    $\mathcal{W} \leftarrow [x]$   $\triangleright$  Update waypoints
4:    $\text{Set\_Waypoints}(\mathcal{W})$   $\triangleright$  Move the drone (Alg. 2)
5:    $i \leftarrow \text{Capture\_Image}()$   $\triangleright$  Capture an image (Alg. 3)
6:    $\text{Receive\_Image}(i)$   $\triangleright$  Transmit image (Alg. 4)
7: end for
8: for  $k \in \{1, 2, \dots, K\}$  do
9:    $\mathcal{W} \leftarrow \text{NBV\_Prediction}()$   $\triangleright$  Predict NBV (Alg. 5)
10:   $\text{Set\_Waypoints}(\mathcal{W})$   $\triangleright$  Move to NBV (Alg. 2)
11:   $i \leftarrow \text{Capture\_Image}()$   $\triangleright$  Capture an image (Alg. 3)
12:   $\text{Receive\_Image}(i)$   $\triangleright$  Transmit image (Alg. 4)
13: end for

```

The flowchart of the system in the right part of Fig. 4, highlights four main sub-processes: *Set Waypoints Process*, *Capture Image Process*, *Receive Image Process*, and *NBV Prediction Process*. Each sub-process is represented by distinct colors in the diagram and described as follows:

- **Setting Waypoints (Alg. 2):** Waypoints for the drone are pre-configured and stored on the ground station. These waypoints are transmitted to the drone through a communication channel comprising a Raspberry Pi, an Android mobile phone connected to the remote controller, and a remote controller. The drone navigates to each waypoint to align with the predicted NBV.

Algorithm 2 Set Waypoints

Require: Waypoints \mathcal{W} , and a drone system \mathcal{D}

- 1: $\mathcal{D}_{gs} \xrightarrow{\mathcal{W}} \mathcal{D}_{pi} \xrightarrow{\mathcal{W}} \mathcal{D}_{ad} \xrightarrow{\mathcal{W}} \mathcal{D}_{ct} \xrightarrow{\mathcal{W}} \mathcal{D}_{drone} \triangleright$ Send waypoints to the drone
 - 2: **for** $w \in \mathcal{W}$ **do**
 - 3: $\mathcal{D}_{drone}.\text{move_to}(w) \triangleright$ Move to waypoint
 - 4: **end for**
-

- **Capturing Images (Alg. 3):** Upon reaching a waypoint, the Raspberry Pi retrieves the drone’s real-time position from the ground station. Once the waypoint is confirmed, the ground station sends a ”capture image” command. The drone then captures the image using adjusted camera parameters.

Algorithm 3 Capture Image

Require: A drone system \mathcal{D}

- 1: **while** $\mathcal{D}_{drone}.\text{loc} \not\approx \mathcal{D}_{pi}.x$ **do** \triangleright Wait until location matches NBV
 - 2: Continue
 - 3: **end while**
 - 4: $\mathcal{D}_{pi} \xrightarrow{\text{NBV_reached}} \mathcal{D}_{gs} \triangleright$ Notify ground station
 - 5: $i \leftarrow \mathcal{D}_{drone}.\text{capture}() \triangleright$ Capture image
 - 6: **return** $i \triangleright$ Return image
-

- **Receiving Images (Alg. 4):** After capturing an image, the drone transmits the image along with its real-time pose back to the ground station. These images are used to iteratively update the reconstruction model.

Algorithm 4 Receive Image

Require: Image i and a drone system \mathcal{D}

- 1: $\mathcal{D}_{drone} \xrightarrow{i} \mathcal{D}_{ct} \xrightarrow{i} \mathcal{D}_{ad} \xrightarrow{i} \mathcal{D}_{pi} \xrightarrow{i} \mathcal{D}_{gs} \triangleright$ Transmit image to ground station
 - 2: $\mathcal{D}_{gs}.\text{save}(i) \triangleright$ Save image
 - 3: $\mathcal{D}_{gs}.\text{save}(x') \triangleright$ Save real-time position
-

- **Predicting the NBV (Alg. 5):** The ground station processes the captured image and the drone’s pose to predict the next-best-view using the NBV module. The newly determined viewpoint is then sent to the drone to continue the data collection process.

Algorithm 5 NBV Prediction

Require: A drone system \mathcal{D}

- 1: $\mathcal{I} \leftarrow [i_1, \dots, i_n] \triangleright$ Load images
 - 2: $\mathcal{X}' \leftarrow [x'_1, \dots, x'_n] \triangleright$ Load positions
 - 3: $\mathcal{G} \leftarrow \mathcal{D}_{gs}.\text{MASt3R}(\mathcal{X}', \mathcal{I}) \triangleright$ Compute grid
 - 4: $x \leftarrow \mathcal{D}_{gs}.\text{pred_NBV}(\mathcal{G}, i_n, x'_n, h) \triangleright$ Predict NBV
 - 5: $\mathcal{W} \leftarrow \mathcal{D}_{gs}.\text{generate_waypoints}(x) \triangleright$ Generate waypoints
 - 6: **return** $\mathcal{W} \triangleright$ Return waypoints
-

Alg. 1 provides an overview of the entire process. Initially, the drone visits three pre-defined viewpoints to synchronize the real-world and virtual-world data (lines 1-7). Following these initial captures, the NBV module predicts subsequent viewpoints based on the collected data (lines 8-13), guiding the drone iteratively until sufficient data is acquired for reconstruction. Additionally, the MAST3R module is integrated into the ground station to convert RGB images into pointmaps (e.g., depth images). By combining these components, the system enables efficient and intelligent data collection, demonstrating the potential of drones as autonomous agents for scalable and versatile real-world scenarios.

K Training and Testing Details

This section includes the details of the training and testing. We employ PPO [89] from stable-baselines3 [90] as the reinforcement learning (RL) framework for Hestia. The grid resolution g is set to 20, and h and w are set to 300. The initial learning rate is 3×10^{-4} and is decayed by a factor of 2 every 500,000 iterations starting from 2,000,000 iterations until reaching 4,000,000, for a total of 5,000,000 training iterations. During training, H_t is randomly sampled from the initial viewpoint height, up to a maximum of 10 meters. For testing, H_t starts at 10 meters, is reduced to 5 meters during the last 10 to 5 steps, and further decreases to 2 meters in the final 5 steps. A training episode ends and the scene resets either when the number of captured images reaches 50 or when the target face coverage ratio of 0.9 is achieved. The complete training process takes approximately 24 hours on an NVIDIA RTX A6000 GPU.

Our network architecture is lightweight, with only 4.9 million parameters (see Tab. A5), which is approximately half the size of a standard ResNet-18 model, which has around 11.7 million parameters. The proposal network consists of three 3D convolutional layers, each followed by a Leaky ReLU activation. This design progressively downsamples the 3D grid before further downstream operations. It is then followed by a 3D self-attention layer, again paired with a Leaky ReLU activation, to expand the receptive field. Finally, the network applies a reparameterization trick module, composed of linear layers, to generate the output distribution parameters. This design allows the look-at point to be sampled from a distribution rather than predicted deterministically. The grid encoder consists of three 3D convolutional layers, each followed by batch normalization and a Leaky ReLU activation. After encoding, trilinear interpolation is applied to each encoded grid feature, followed by feature concatenation. The image encoder is composed of three 2D convolutional layers, each followed by batch normalization and Leaky ReLU activation. The encoded features are then flattened and passed through a linear layer with Leaky ReLU activation. For the policy network, we adopt the default model provided in stable-baselines3. For more details about the network architecture, please refer to the code provided in the supplementary materials. The hierarchical design first predicts the look-at point, followed by the camera position. This design prioritizes the look-at point, as the primary objective in this task is to determine where to look rather than where to fly. It also resembles how a human pilot controls a drone during data capture, focusing first on the target of observation before planning the flight path.